Research Article

Luminescence chronology of fluvial and aeolian deposits from the Emirate of Sharjah, UAE

Daniela Mueller[a]* (iD), Kira Raith[b]* (iD), Knut Bretzke[c] (iD), Alexander Fülling[a], Adrian G. Parker[b] (iD), Ash Parton[d] (iD), Gareth W. Preston[b] (iD), Sabah Jasim[e], Eisa Yousif[e] and Frank Preusser[a] (iD)

[a]Institute of Earth and Environmental Sciences, University of Freiburg, Freiburg, Germany; [b]Human Origins and Palaeoenvironments Research Group, School of Social Sciences, Oxford Brookes University, Oxford, United Kingdom; [c]Department of Early Prehistory and Quaternary Ecology, University of Tübingen, Tübingen, Germany; [d]Mansfield College, University of Oxford, Oxford, United Kingdom and [e]Sharjah Archaeology Authority, Government of Sharjah, Sharjah, United Arab Emirates

Abstract

Quaternary environments on the Arabian Peninsula shifted between pronounced arid conditions and phases of increased rainfall, which had a profound impact on Earth surface processes. However, while aeolian sediment dynamics are reasonably well understood, there is a lack of knowledge with regard to variability in the fluvial systems. Presented here are the findings from several locations within wadi drainage systems to the west of the Hajar Mountains (United Arab Emirates). The performance of optically stimulated luminescence dating using a customized standardized growth curve approach is investigated, showing that this approach allows reliable determination of ages by reducing the machine time required. Three main periods of fluvial activity occurred at 160–135, 43–34, and ca. 20 ka. Additional ages fall into the latest Pleistocene and Late Holocene. None of the ages coincides with major wet periods in SE Arabia that have been identified in stalagmites and by the deposition of lake sediments. It is shown that fluvial activity was partly contemporaneous (within the given time resolution) with phases of aeolian deposition and was almost continuous, but likely sporadic, during the Middle to Late Pleistocene. This highlights the need for regionally defined paleoenvironmental records to fully understand the response of dryland systems to long-term climatic change.

Keywords: Luminescence dating, Quartz, Fluvial-aeolian sediments, Arabia, Quaternary

(Received 1 March 2022; accepted 24 August 2022)

INTRODUCTION

Quaternary environmental change on the Arabian Peninsula has been characterized by shifts between pronounced arid conditions and phases of increased rainfall, the latter caused by strengthening of monsoonal circulation (Burns et al., 1998, 2001, Fleitmann and Matter, 2009). While during arid phases the landscapes of Arabia resemble desert environments dominated by transport and deposition of aeolian sand (Goudie et al., 2000; Preusser, 2009; Atkinson et al., 2012; Farrant et al., 2015), the amount of precipitation during wetter phases was sufficient to support savannah vegetation with permanent lakes and wetlands (Rosenberg et al., 2011, 2012, 2013; Parton et al., 2015a, 2018; Engel et al., 2017). Another feature reflecting hydroclimatic changes is the widespread occurrence of fluvial sediments (Maizels, 1987; Maizels and McBean, 1990). These are particularly extensive along the western Hajar Mountains (Fig. 1), however, the number of independently dated fluvial deposits in Arabia is low, often with large distances between sites and variation across spatial and temporal

records (Anderson, 2007; Blechschmidt et al., 2009; McLaren et al., 2009; Parker, 2010; Delagnes et al., 2012; Farrant et al., 2012; Atkinson et al., 2013; Parton et al., 2013, 2015a; Hoffmann et al., 2015; Matter et al., 2016). Furthermore, few attempts have been made in this region so far towards systematic tracing of fluvial dynamics from source to sink along entire fluvial (wadi) drainage systems. Understanding fluvial records and the interaction between fluvial and aeolian environments, however, requires consideration of surface processes that occurred during the late Quaternary, including patterns of debris supply, transport, and accumulation (Guba and Glennie, 1998). These are profoundly influenced by bedrock lithology and structure, which determine the nature of debris supply and location accommodation space by which alluvial and fluvial systems form.

The dating of fluvial records offers the possibility to detect changes in hydroclimate dynamics, including under arid conditions, that are not necessarily captured in speleothem records. The latter are terrestrial proxies that rely on sufficient rainfall (∼350 mm of annual precipitation) to initiate growth (Vaks et al., 2010; Fleitmann et al., 2011) and are compromised or absent during periods of increased aridity. As such, there is a considerable range of rainfall that remains undetectable from these records. Such levels of rainfall might be insufficient for the formation of particularly large water bodies and speleothem growth, yet
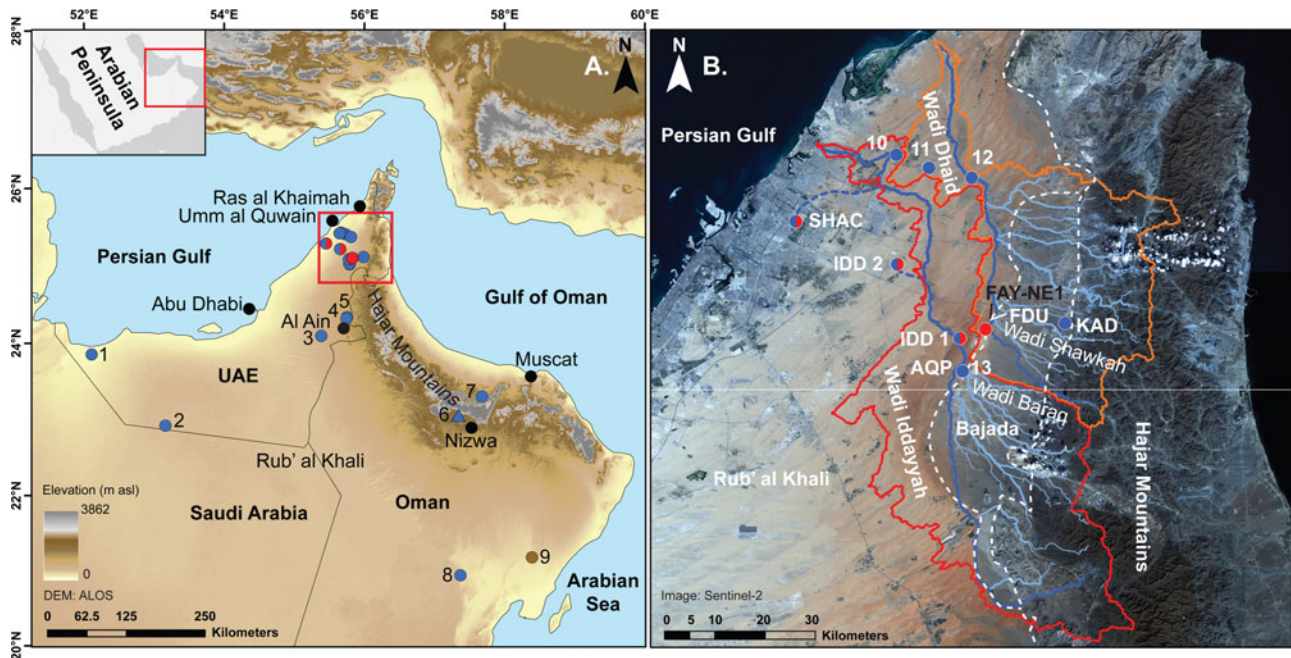
Figure 1. Location of the wider study region (**A**) and the Wadi Iddayyah and Wadi Dhaid catchments (**B**). Modern (blue lines) and paleo-drainages (dashed blue lines) are shown for the catchments of Wadi Iddayyah (delineated in red) and Wadi Dhaid (delineated in orange). White dashed lines denote the extent of the mountain front and bajadas. Regional paleofluvial (blue circles), speleothem (blue triangle), aeolian (red circles), paleosol (brown circle), and both paleofluvial and aeolian (red/blue circles) records and locations are shown as mentioned in the text: 1. Sabkha Matti; 2. Liwa; 3. Remah; 4. Sibetah; 5. Al Ain; 6. Hoti Cave; 7. Wadi Mistal; 8. Saiwan; 9. Al-Mamla, Wahiba; 10. Mohadeb; 11. Tawi Asmar; 12. Fallaj al Moalla; and 13. Aqabah.

capable of triggering the widespread activation of ephemeral drainage networks within the upper catchments (proximal), medial drainage areas, and lower (distal) end members.

Occupying an area of 600,000 km², the Rub' al-Khali is the largest sandy desert on Earth (Besler, 1982; Goudie, 2002). While this region is largely characterized by aeolian dune systems, it also features an extensive paleo-drainage network (Edgell, 2006). Previous work on fluvial sediments, though limited in nature, provides some insights into the chronology of wadi activation and sediment deposition. In central Saudi Arabia, fluvial deposits were deposited during short-lived wetter periods at ca. 54, ca. 39, and ca. 0.8 ka (McLaren et al., 2009). Using a combination of radiocarbon and optically stimulated luminescence (OSL) dating, Matter et al. (2016) demonstrated the presence of perennial streams and a permanent freshwater lake in the distal reach of the Dawasir drainage system in the Rub' al-Khali desert region of Saudi Arabia, synchronous with fluvial accumulation in the headwaters of its major tributary, Wadi Tathlith. Increased runoff during the Early Holocene (10–6 ka) led to a re-activation of streams that largely followed pre-existing Pleistocene courses. In Wadi Sana, Yemen, Anderson (2007) dated fluvial sediment deposition between 12 and 7 ka, with continued aggradation until ca. 5 ka.

In southeast (SE) Arabia, Atkinson et al. (2013) demonstrated that phases of alluvial and fluvial activation occurred in marine isotope stage (MIS) 5e (ca. 130–115 ka), 5a (ca. 90–76 ka), and the Early Holocene. The fluvial Hili Formation shows evidence for perennial river flow during MIS 5e and 5a, with channels up to 20 m across and water depths of at least 2 m. In addition, extensive accumulation of fan gravel occurred at the mountain front (Atkinson et al., 2013; Farrant et al., 2015; Parton et al., 2015b) and apparently reaches back several 100 ka (Blechschmidt et al., 2009).

The aim of this study is to provide additional chronological data using OSL dating to further decipher the complex interplay of Quaternary alluvial, fluvial, and aeolian sedimentary systems in SE Arabia. However, OSL dating of fluvial sediments has been proven to be sometimes challenging due to the problem of partial bleaching (see Wallinga, 2002; Rittenour, 2008). In order to distinguish grains on aliquots that have been affected by partial bleaching, a statistical approach is used to identify the fraction of aliquots in which the signal was fully reset at the time of deposition for which a sufficient number of aliquots has to be measured (Galbraith and Roberts, 2012). This is an elaborate and time-consuming process, which can be significantly reduced by the application of a standardized growth curve (SGC) approach (Li et al., 2015, 2016). This approach uses the full single aliquot regenerative dose (SAR) protocol (Murray and Wintle, 2000) only for a limited number of aliquots while the remaining aliquots are measured with a reduced protocol. The aim of this procedure, which is to reduce the measuring time without compromising accuracy or precision, was shown to reduce measurement times by up to 70% (Mueller and Preusser, 2022). The SGC method was first proposed for luminescence dating by Roberts and Duller (2004), and has since been refined and applied for the dating of sediments from a broad range of environmental contexts (e.g., Hu et al., 2019; Fu et al., 2020; Mueller and Preusser, 2022). Nevertheless, as yet there has been no systematic work published using this approach on sediments from Arabia.

To achieve the ultimate goal of the study (i.e., improve the understanding of Quaternary sedimentary system dynamics in response to climate change), we first focus on assessment of the luminescence properties and measurement protocol performance, and verify application of the SGC approach from sediments along the proximal, medial, and distal end members of two wadi systems in the United Arab Emirates (UAE). The new data are then discussed in the context of previously published information regarding the timing of both environmental change and sedimentary dynamics in SE Arabia.

Regional setting and site description

SE Arabia (Fig. 1) lies at the interface between the hot desert climate of the Rub' al-Khali desert and the Hajar (Oman) Mountains (Parker et al., 2004). The region is influenced by both the mid-latitude Westerlies and the Indian and African monsoons, which form part of one of the most dynamic climate systems on the planet (Clemens et al., 1991). Consequently, SE Arabia is a key region for assessing hydroclimatic changes at the monsoon-westerly interface during the past. The area is located north of the summer position of the Intertropical Convergence Zone, with monsoon-sourced rainfall presently limited to southern and western margins of the Arabian Peninsula (Parker and Goudie, 2008; Herold and Lohmann, 2009; Jennings et al., 2015; Parton et al., 2015a).

The Hajar Mountains are characterized by steep relief, low rainfall, and high evapotranspiration (Parker et al., 2004). The maximum elevation, the Hajar at Jebel Shams in Oman, is 3028 m asl (Fig 1b), whereas the maximum elevation in the catchments of the study area is 2042 m asl. Although much of the mountain area has little or no vegetation cover, it does represent a center of relict biodiversity with strong floristic ties to southwest Asia, but is now isolated from this area by the Arabian Gulf and the lowland desert areas (Ghazanfar, 1991). Farther to the south in Oman, where the topography exceeds 2000 m asl, there is a sufficient elevation change to represent a significantly different climate zone, with associated floral changes in comparison to the desert lowlands areas (Ghazanfar, 1991). Rainfall enhanced by the orographic effects of the Hajar Mountains occurs in the winter months (December to February) and is associated with mid-latitude Westerlies (Fisher and Membery, 1998) that originate as cyclonic depressions in the eastern Mediterranean, penetrating into the Persian Gulf, and hemmed in by the Zagros Mountain range in Iran to the north (Parker et al., 2004; Parton et al., 2015b). Rainfall is characteristically low (~120 mm/yr), with a strong precipitation gradient across the region between the Hajar Mountains (~140 mm/yr) and Abu Dhabi (<50 mm/yr) (Parker and Goudie, 2008; Pain and Abdelfattah, 2015). The wind regime across the region is complex, with 52% of sand-moving winds blowing from the west and northwest, driven by Shamal winds, 28% of sand-moving winds blowing from the southeast, and the remainder across a range of directions (Goudie et al., 2000; White et al., 2001).

Within the study area, the geology of the Hajar Mountains is dominated by a Late Cretaceous Ophiolite succession, including mantle peridotites, typically harzburgite, and gabbros, with some polydeformed metamorphic rocks. On the western flank of the mountains, Late Cretaceous to Paleogene shallow water marine limestones are found (Thomas et al., 2006).

A series of coalesced alluvial fans (bajadas) of Miocene to Quaternary age forms a vast geomorphic system that stretches along the southwestern margin of the Hajar Mountains from the northern UAE (Al Farraj and Harvey, 2000, 2004, 2005; Farrant et al., 2006, 2012) through northern Oman (Abrams and Chadwick, 1994; Blechschmidt et al., 2009) to the Wahiba Sands (Maizels, 1987) (Fig. 1). In the UAE, these bajadas are largely of Quaternary age and mainly constructed of gravel deposits; but in northern Oman, most of the system consists of a dissected older fan sequence of Miocene to Pliocene age (Macklin et al., 2012) that is locally buried beneath more recent Quaternary gravels (Blechschmidt et al., 2009). Under current climatic conditions, these bajadas are almost completely inactive, with only minor surface reworking and channel incision occurring during rare flood events (Al Farraj and Harvey, 2004; Farrant et al., 2012; Parton et al., 2015b). The largest fans occur in northern Oman (Abrams and Chadwick, 1994; Blechschmidt et al., 2009), where a vast alluvial plain consisting of coalescing low-gradient (<0.3°) fans exceeding 100 km in length formed along the southwestern margin of the Hajar Mountains. In the UAE, the Quaternary fans form an array of almost continuous deposits between Al Ain and Ras al Khaimah (Fig. 1), which are in some places ~50 m thick (Al Farraj and Harvey, 2004; Parton et al., 2015b). The size and morphology of the Quaternary alluvial fans depend on the size of the catchment area, climate, and the dominant lithology of the fan gravels. The local geology, the steep relief of the Hajar Mountains, and the low frequency but high intensity nature of the flooding of the watercourses are key in the formation of the distinctive wadi geomorphology and series of fluvial/alluvial deposits (Parker and Goudie, 2008).

Wadi systems drain into the Rub' al-Khali dune field, which is the largest active sand sea in the world, covering ~560 000 km² (White et al., 2001). The dunes in this part of the Rub' al-Khali mostly comprise linear megaridges, up 80 m high, formed initially by winds blowing from southwest to northeast. Under current wind conditions, however, the megadunes are more or less transverse to the prevailing shamal winds, so that the linear megaridges are overlain by secondary patterns (Goudie et al., 2000; Farrant et al., 2015). Dune geochemistry has revealed the mixing of two major sources of sediment: a terrestrial source of reddened quartz grains, and a marine carbonate source (White et al., 2001). Material derived from fluvial sources, originating from the mountains, contributes only a minor component into the dune field owing to the low quartz components found in regional limestone and mantle rocks (Garzanti et al., 2013). The major source for the dune sands comes from reworked carbonate-rich Pleistocene aeolianite from as far as 80 km inland, or from Miocene siliciclastic strata coming from the west (Farrant et al., 2015). Within the study area, the linear megaridges of the dune system are truncated or disrupted by several wadi courses.

For this study, two Wadi systems (Wadi Iddayyah and Wadi Dhaid) and a dune adjacent to the archaeological site at Jebel Faya (FAY-NE1) (Armitage et al., 2011) were investigated (Fig. 1). The dune (FDU) is located at the foot of Jebel Faya, which is part of the 20 km Al Faya anticline, a limestone outlier of the Hajar Mountains, and was sampled to characterize the nature of dune sediments from a fresh exposure in close proximity to the wadis. The site, situated between the Persian Gulf in the west and the Gulf of Oman in the east, is ~60 km inland from either coast. The headwaters of both wadi systems are located in the Hajar Mountains. In the piedmont area, a series of extensive, low gradient, alluvial fans coalesce along the western margin of the Hajar Mountains, forming a vast system, which extends up to 20 km westward from the mountain front. The fans spread out towards the Jebel Faya Anticline where alluvial channels merge into wadi systems. From the apex of the alluvial fans, the main wadi systems split to form a complex series of anastomosing as well as braided distributary channels that keep their form for several kilometers before becoming more diffuse in the mid-portion of the fan. The wadis vary in width, but are typically tens of meters wide with flat floors. The channels tend to be braided with lenses of finer-grained material, while coarser gravels and boulders extend across the wadi floors, especially in the proximal part of the fluvial systems. Along the wadi systems, clast size

generally decreases downstream of the alluvial fans, where the material in active transport is generally fine gravel and sand.

Wadi Iddayyah, the main drainage system within the Jebel Faya Anticline area, extends >170 km from its headwater source in a northwest direction towards the coast, but terminates in the desert ~30 km before reaching the Gulf. En route, it passes to the west of Jebel Aqabah and Jebel Faya (site FDU) where the channel merges with its main feeder channel, Wadi Baraq (Parton et al., 2013; site AQP of this study; Fig. 1). Together the two systems then run as a single channel in a northwest direction through the Rubʿ al-Khali dune field (IDD1 and IDD2, this study) towards the Persian Gulf coast (SHAC, this study). Approximately 20 km to the north, the neighboring wadi system of Wadi Dhaid flows from the Hajar Mountains in the UAE for ~102 km in approximately the same northwest direction as Wadi Iddayyah.

Unlike Wadi Iddayyah, Wadi Dhaid reaches the Persian Gulf. It is fed by the large braid plains featuring several fluvial systems, including Wadi Shawkah (KAD, this study; Fig. 1), Wadi al-Yitaymah, and Wadi al-Qorad, which merge to form a larger wadi course that flows northwards for several kilometers along the western edge of the inland basin towards Wadi al-Dhaid/ Wadi Madsah (Drechsler, 2008). The middle and lower parts of Wadi Dhaid, locally termed Wadi Limhah, cuts through the dunes and meets the sea to the north of Umm al Qaiwain. However, it is evident from exposures at Tawi Asmar (25°25′N, 55°45′E) (Atkinson et al., 2013) and at a series of oases at Fallaj al Moalla and Mohadeb, that wadi gravels underlie large tracts of the dune field (Farrant et al., 2006; Parker and Rose, 2008; Parker, 2010). The gravels were deposited under conditions of higher runoff and sediment transport than occur today. Such past depositional regimes were likely far more consistent than today, because even under modern flash flood conditions, the middle and lower stretches of these wadis are inactive while the deposition of cohesive, stratified sediments is almost entirely absent.

Within both wadis, the proximal part of the alluvial fan system is characterized by a small number of deeply incised alluvial channels, up to 5–10 m into the fan surface. The gravel deposits here are usually extremely poorly sorted and are generally massively bedded channel fills and debris flows with occasional cut-and-fill structures. The deposits generally contain very few sedimentary structures other than imbrication and channels. Farther down the fans, gravels contain both stream-flow and sheet-flood sediments, typically characterized by 1–5 m thick, graded, fining-up sequences and channelized beds of gravel, interbedded with coarse, cross-bedded ophiolite-dominated gravelly sand. Sheet-flood deposits, which become increasingly common lower down the fan, consist of gravel/sand couplets that display both planar and trough cross-bedding. In the medial parts of the wadi systems, the sediment is typically dominated by medium- to coarse-grained, moderately sorted sand, locally interbedded with fine gravel, fine-grained sand, or laminated silt. There is an increase in the component of quartz derived/reworked from the surrounding dune fields. The distal end of the wadi systems largely comprises sand and silt of sheet-flood origin with sedimentary structures associated with ephemeral streams, including climbing ripples, rip-up clasts, slump structures, collapsed blocks from channel undercutting, erosional channel cut and fill features, cross-bedding, and planarbedding. Locally, beds of fine-grained sand and silt with mud cracks and curls occur, representing waning flow and desiccation. Much of the sediment appears to be reworked quartz-rich aeolian sand from the surrounding dune field rather than being derived from the ophiolite rocks in the headwaters of the catchment,

with coarser lithic grains and many rip-up clasts of laminated silt (Farrant et al., 2006). Locally the sand is derived from three sources: (1) transported down from the mountains by fluvial action; (2) eroded from the underlying bedrock (often cemented calcarenites from alluvial fan sand or cemented aeolianite); and (3) a significant aeolian component of fine- to medium-grained, sub-rounded sand, blown in from the neighboring dune-fields. Clast size generally decreases downstream, and downstream of the alluvial fans, the material in active transport is bed-load dominated and generally consists of fine gravel and sand.

The locations of sampling sites are shown on Figure 1 and sedimentary logs are provided in Figure 2. Samples were collected from the proximal part of Wadi Dhaid and medial and distal parts of Wadi Iddayyah from quarry and natural exposures cutting through exposed alluvial/fluvial and aeolian sediment deposits. In addition, samples were collected from a dune exposure on the flank of Jebel Faya. At each site, the sediment units were logged and described in detail in the field and samples collected for sedimentological analyses and for age determination (Table 1, see Supplementary Figs. 1–6 and Supplementary Tables 1–8 for details of each site).

MATERIAL AND METHODS

Samples and sample preparation

Twenty-two samples were obtained at six sites (Figs. 1, 2; Table 1), including outcrops (IDD1, IDD2, AQP, SHAC), an excavated trench (FDU), and a gravel pit (KAD). For this, the surfaces were cleaned and opaque plastic tubes were driven horizontally into the exposures at most sites. Due to sediment cementation, three blocks of sediment (SHAC2, SHAC4, SHAC6) were cut out of one outcrop and covered in opaque wrap. At site KAD, deposits predominantly consist of gravel, so to increase the amount of sediment collected in the preferred grain size range for OSL dating, sample material was pre-sieved in the field. Therefore, sampling was conducted at night, material was removed from the exposure, sieved, and only the <200 µm fraction was transferred to opaque bags. For this site, additional bags with pristine, un-sieved material were collected for dose rate determination.

All samples were opened and handled under subdued red-light conditions at the Freiburg Luminescence Laboratory (Germany). Tube ends (3–4 cm) and the outer rind of the block samples were removed, dried, and pulverized for dose rate determination. Collected bags for KAD were processed equally.

The remaining material was prepared for equivalent dose (D_e) determination following standard laboratory procedures, including wet-sieving, carbonate removal with 20% hydrochloric acid (HCl), and density separation using sodium polytungstate (<2.70 g/cm^3; >2.58 g/cm^3) to isolate the quartz fraction. Quartz grains were etched in 40% hydrofluoric acid (HF) for one hour to remove the alpha-irradiated rinds and any remaining feldspar grains. Any fluorides that may have precipitated during this process were dissolved by one hour treatment with 20% HCl. Purified and dried quartz grains (100–150 µm, 150–200 µm; Table 2) were mounted onto stainless-steel cups using silicon oil stamp with a diameter of 2 mm (~170 and 90 grains, respectively).

Measurement equipment and protocols

D_e values were obtained with a Freiberg Instruments Lexsyg Standard reader (Richter et al., 2013) using LEDs with peak
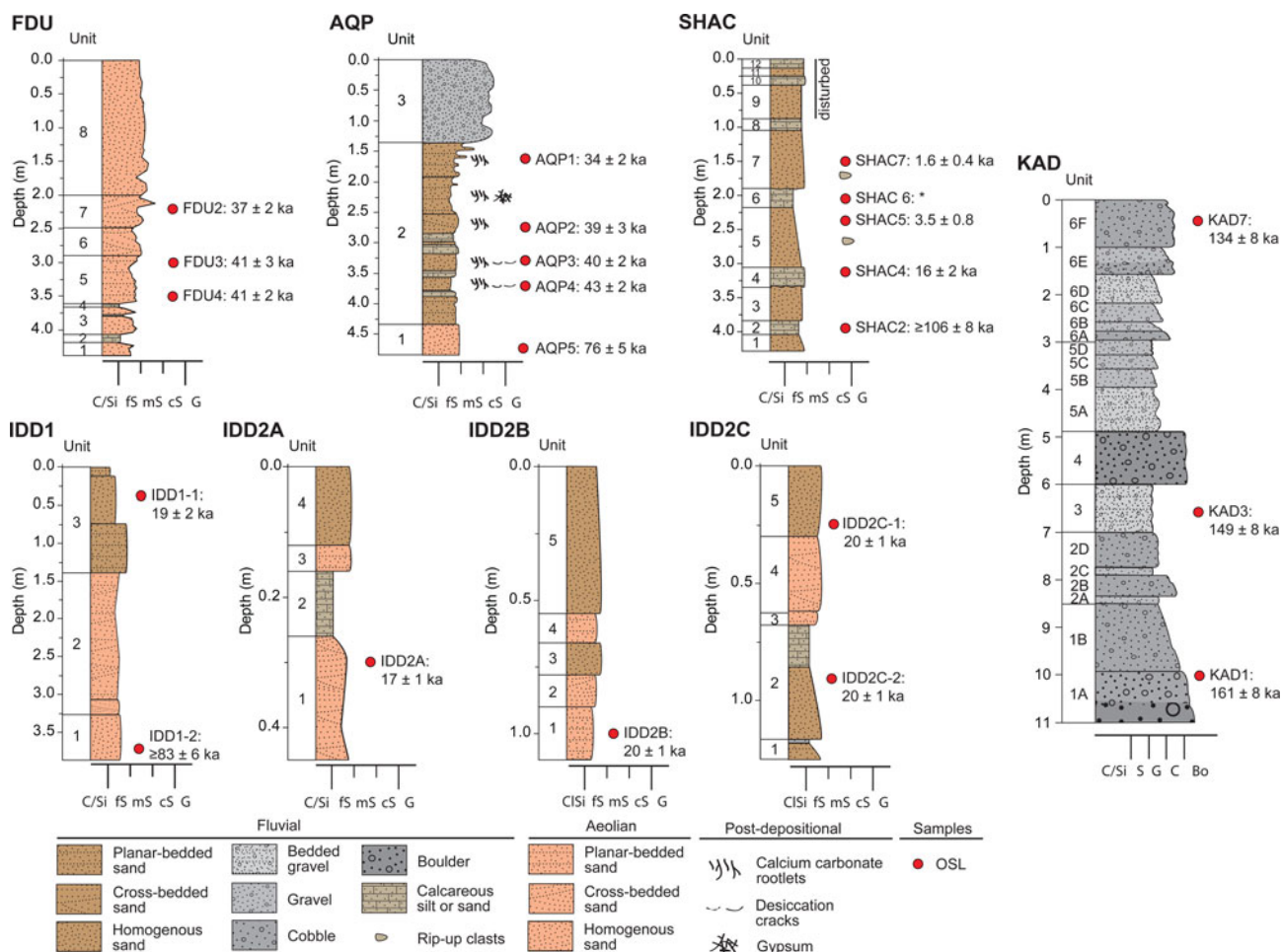
Figure 2. Sediment logs of all investigated sites. Note, y- and x-axes vary for each of the shown logs (C/Si = clay/silt; S = sand; G = gravel; C = cobbles; Bo = boulders). OSL ages are given as described in the text. *The derived age for SHAC6 was rejected (see subsection "Luminescence chronology").

emission at 525 nm (green range). The emitted OSL signals were detected by an H7360-02 photomultiplier tube filtered through a 3 mm BG 39 Schott glass and a 5 mm Delta-BP 365/50 EX-interference filter. Laboratory irradiation was given by a ^{90}Sr/^{90}Y beta source mounted into the reader. The beta source was calibrated using LexCal2014 calibration quartz (90–160 µm; 3 Gy) to ~0.07 Gy/s.

All measurements were conducted using preheating prior to the natural (L_n), regenerative (L_x) and test doses (T_n, T_x) for which the aliquots were heated at 5°C/s to the preheat temperature and held for 10 s. An adequate preheat temperature combination of 260°C (L_n, L_x) and 200°C (T_n, T_x) was found. For the ease of reading, details of performance tests and their results are given in section "Luminescence properties and performance." D_e measurements were conducted following the SAR protocol (Murray and Wintle, 2000) with a test dose of ~14 Gy. Full SAR measurements were performed on 7–12 aliquots per sample (Supplementary Table 9). Aliquots that suffered from poor recycling, depletion after infrared stimulation (>20%), or recuperation issues (L_x/T_x [0 Gy dose] >5% of L_n/T_n) were rejected (Supplementary Table 9). In addition, poor fitting of the dose response curve (DRC) as determined by the figure of merit (FOM) was applied as a rejection criteria. Following Peng and Li (2017), an FOM of <10 indicates an accurate fit of the DRC. The FOM is a measure of goodness-of-fit ($FOM = \Sigma|y_i^f - y_i^f| / \Sigma y_i^f * 100$) that accounts for the normalized

differences between observed (y_i^o; L_x/T_x) and fitted (y_i^f; DRC) data. The SAR dataset was subsequently used to determine a SGC for each sample following Li et al. (2016). For this, the SAR datasets were least-square (LS) normalized by iteratively scaling and fitting of L_x/T_x (for details see Li et al., 2016) and fitted with a single-saturating exponential function.

In addition to the SAR dataset, simplified measurements (SM) were conducted on 31–43 aliquots per sample (Supplementary Table 9). This reduces the measurement time for one aliquot by ~60%. The SM dataset consists of the L_n/T_n and one L_x/T_x measurement (~55 Gy) of each aliquot. The latter was used to individually re-normalize the SGC and L_n/T_n value for every measurement. To account for uncertainty of the SGC, the average deviation of the established SGC is combined in quadrature with the uncertainty of L_n/T_n to calculate the D_e uncertainty. D_e values were then determined for both the SAR and SM datasets. L_n/T_n measurements that failed to intersect with the SGC were regarded in saturation, are listed in Supplementary Table 9, and were rejected from D_e determination.

While performance of the SGC was assessed for all samples, SAR performance was investigated in depth for one expectedly well-bleached aeolian sample (FDU2). In addition, the chosen SAR protocol was tested for one representative sample per site to verify the regional applicability. Decay curves were assessed and the initial signal was set to be derived from the first 1 s of

Table 1. Overview of sampling sites, samples, facies, and depositional environments.

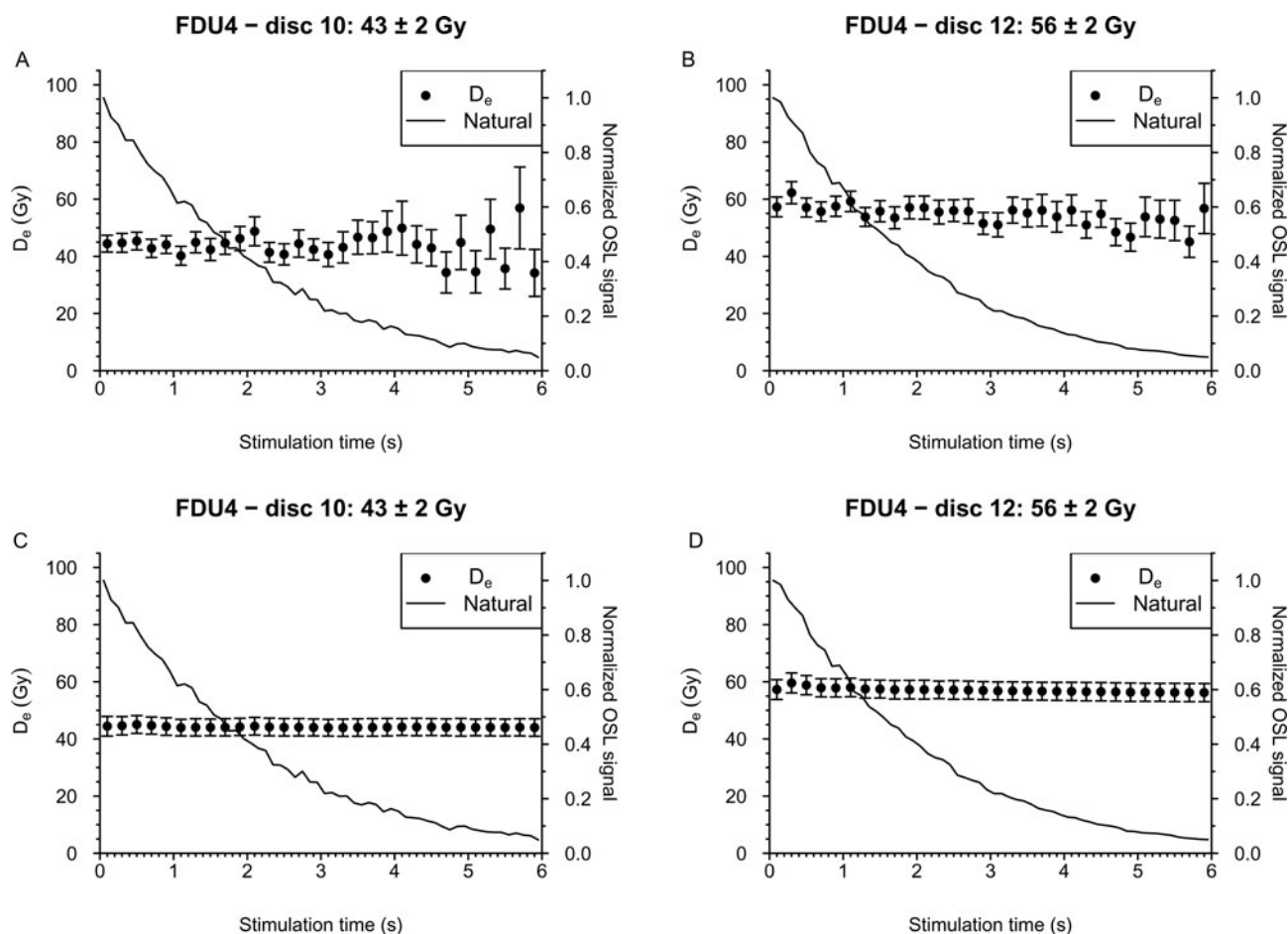| Site	Coordinates	Sample code	Depth (m)	Facies	Depositional environment
FDU	25.12°N, 55.85°E	FDU2	2.2	Fine-grained, cross-bedded sand	aeolian
		FDU3	3.0	planar-bedded sand	aeolian
		FDU4	3.6	planar-bedded sand	aeolian
KAD	25.13°N, 56.01°E	KAD1	10.0	serpentine clasts in poorly sorted, coarse-grained matrix (sand, gravel, cobbles)	fan deposit, fluvial
		KAD3	6.5	planar bedding with alternating fine beds of ophiolite fine gravels and sands cemented with hydromagnesite or silcrete	fan deposit, fluvial
		KAD7	0.5	sequence of planar-bedded gravels with fining-upwards trend and sand in matrix	fan deposit, fluvial
AQP	25.04°N, 55.80°E	AQP1	1.9	planar-bedded silts and reworked aeolian sand	fluvial
		AQP2	3.4	cross-bedded silts and reworked aeolian sand	fluvial
		AQP3	3.7	homogenous silts and reworked aeolian sand	fluvial
		AQP4	4.1	planar-bedded silts and reworked aeolian sand	fluvial
		AQP5	4.8	homogenous sand	aeolian
IDD1	25.11°N, 55.78°E	IDD1-1	0.3	homogenous and bedded, reworked aeolian sand	fluvial
		IDD1-2	3.8	homogenous, fine-grained sand	aeolian
IDD2A	25.23°N, 55.67°E	IDD2A	0.3	cross-bedded sand	aeolian
IDD2B	25.23°N, 55.67°E	IDD2B	1.0	planar-bedded, fine-grained sand	aeolian
IDD2C	25.23°N, 55.67°E	IDD2C-1	0.2	homogenous sand, fining-upwards	fluvial
		IDD2C-2	0.9	homogenous, fine-grained, reworked aeolian sand	fluvial
SHAC	25.30°N, 55.47°E	SHAC2	4.3	cemented, fine silts and fine-grained sands	fluvial
		SHAC4	3.4	cemented, fine silt with rip-up clasts, fining upwards	fluvial
		SHAC5	2.4	coarse- to medium-grained, poorly sorted sands with large rip-up clasts and ophiolite gravel	fluvial
		SHAC6	2.0	cemented silts and fine-grained sand	fluvial
		SHAC7	1.8	relatively homogenous, coarse-medium sand with some silty rip-up clasts	fluvial

Figure 3. $D_e(t)$ plots of two representative aliquots of FDU4. D_e values were derived from either successive 0.2 s intervals with stimulation time (**A, C**) or for intervals with integration limits that were subsequently extended by 0.2 s (**B, D**).

the OSL decay from which the last 15 s were subtracted (see subsection "Signal properties"). SAR and SGC D_e values were calculated using the numOSL package for R (Peng and Li, 2017; Peng et al., 2018) and age models (central age model [CAM] and minimum age model [MAM]; Galbraith et al., 1999) were applied with the Luminescence package for R (Burow 2020a, b). For the MAM, an expected overdispersion (σ_b) of the well-reset proportion of the sample of 20% is assumed.

For dose rate determination (DR), radionuclide concentrations were determined by high-resolution gamma-ray spectrometry at VKTA (Dresden, Germany; Supplementary Table 10). No evidence for radioactive disequilibrium was reported (Degering and Degering, 2020). The cosmic contribution was determined for present-day depths (i.e., overburden) following Prescott and Hutton (1994). A representative long-term water content of 3 ± 3% was assumed and used for DR determination of all samples, which was calculated together with the OSL ages using ADELE 2017 software (Degering and Degering, 2020).

LUMINESCENCE PROPERTIES AND PERFORMANCE

Signal properties

Quartz grains from all investigated sites presented bright OSL signals (T_n signal > 3 × background, T_n error <20%). However, the green light stimulated decay signals only reduced to ∼20%

after ca. 3 s and $D_e(t)$-plots (Bailey, 2000) were produced to ensure that only the fast component is used to determine D_e values. For this, D_e values were determined for (1) 0.2 s intervals with stimulation time, and (2) for intervals with integration limits that were subsequently extended by 0.2 s. Results for two representative aliquots of FDU4 (Fig. 3) show that D_e values derived over the first 6 s of the signal are consistent. Neither interval position nor interval length have a significant influence on D_e determination, which indicates that the signal is dominated by the fast component. Integration limits for the initial signal were set to the first 1 s of the OSL decay over which the D_e value determination was most consistent. In addition, a late background subtraction using the last 15 s of the signal was applied.

SAR performance tests

At first, performance tests were conducted in depth on one representative aeolian sample (FDU2) that is thought to have been well bleached and to provide insights into the expected spread of D_e values. SAR performance was assessed by the means of three tests: (1) preheat plateau, (2) dose recovery (∼28 Gy given dose), and (3) thermal transfer (Fig. 4). These tests were conducted for three different preheat temperatures for L_x (220, 240, 260°C) with preheats of 200°C for T_x (5°C/s, held for 10 s). For preheat plateau and dose recovery tests, seven measurements
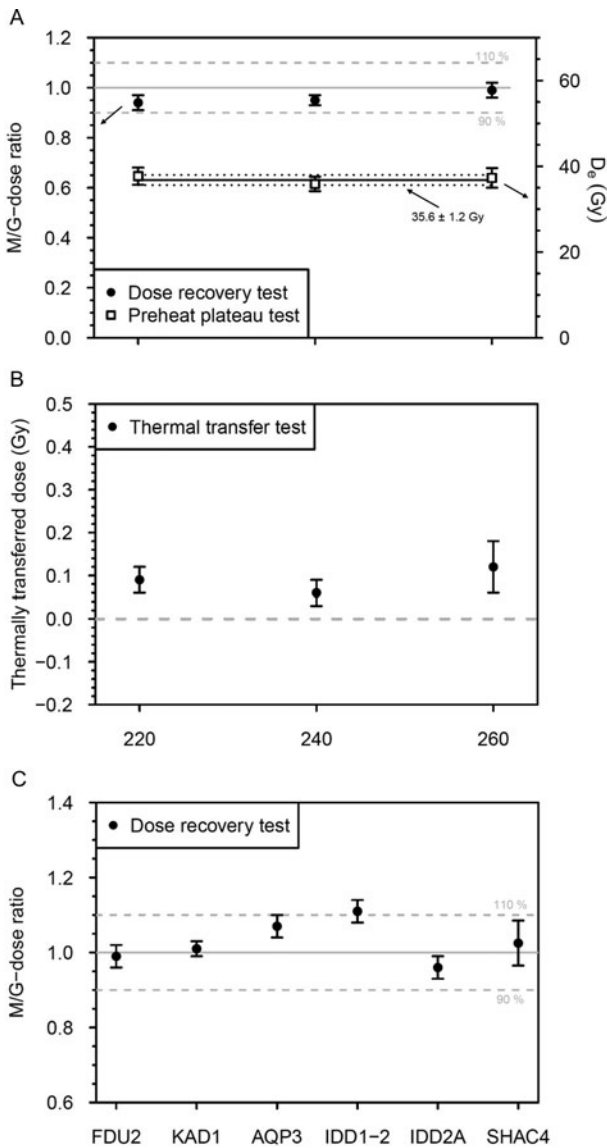
Figure 4. (**A**) Dose recovery (28 Gy given dose; M/G-dose ratio shows the measured-to-given dose ratio) and preheat (PH) plateau test results of FDU2 (mean at 35.6 ± 1.2 Gy). Arrows indicate the y-axis referred to by each dataset. (**B**) Thermal transfer test results of FDU2; the dashed line indicates 0 Gy. (**C**) Dose recovery test results for one sample of each site for a preheat temperature of 260°C.

per preheat temperature combination were performed while three aliquots were used for the thermal transfer test. The preheat plateau test was conducted on the natural signal; both other tests were carried out on sample material that was bleached three times successively for 200 s with green LEDs in the Lexsyg Standard reader.

Natural D_e values and measured-to-given dose (M/G-dose) ratios are consistent across all tested preheat temperature combinations, with the best recovery for a preheat of 260°C (0.99 ± 0.03) and a mean D_e value of the natural at 35.6 ± 1.2 Gy. Thermal transfer is observed for all preheat combinations and ranges between 0.06 ± 0.03 Gy and 0.12 ± 0.06 Gy. However, this equates to <1% of the final D_e values for most samples and is regarded as negligible. Due to the best recovery results, a preheat combination of 260°C for L_x and 200°C for T_x was subsequently chosen. Further dose-recovery tests were conducted on six aliquots of one

representative sample per site using the chosen preheat combination (Fig. 4). M/G-dose ratios were consistent with 1.00 ± 0.10 for all samples, confirming the applicability of the chosen SAR protocol.

SAR dose response curve shapes

Distinctly different DRC shapes have been observed for quartz samples in some (see Li et al., 2016; Hu et al., 2019, 2020; Fu et al., 2020), but not all, recent studies (Mueller and Preusser, 2022). Hence, it is essential to assess the characteristic shapes of the obtained DRCs prior to SGC construction. Li et al. (2016) suggested deriving the ratio between two regenerative dose points, the so-called signal growth ratio (SGR), and to evaluate the spread. Accordingly, SGRs were determined for all SAR measurements of this study using the two highest regenerative dose points. Differences of SGRs per sample range between 12–52% (Fig. 5). Much higher values of ∼200% differences were reported for single-grain measurements by Hu et al. (2019, 2020) and Fu et al. (2020), and ∼90% for aliquots by Li et al. (2016). Mueller and Preusser (2022) found a spread of 30% for samples from Switzerland. This was regarded as evidence for the lack of different DRC types, and hence, as negligible. Therefore, no type-specific SGCs and only a single SGC were calculated for each sample. The SGR spread observed here is rather small and can be reduced by LS-normalization during SGC determination (see subsection "SGC performance"). Additionally, D_e values of most samples are <50 Gy, a threshold below which only one shared shape of DRCs has been reported (e.g., Li et al., 2016; Fu et al., 2020). Hence, only one SGC was derived using all SAR measurements for each sample.

SGC performance

For SGC determination, regenerative dose points of the SAR measurements were LS-normalized (Fig. 6), thereby significantly reducing scatter before being described by the SGR. SGCs are well fitted with single-saturating exponential function giving FOM values between 3.0–9.0, with an average fitting error <0.02 (Table 3). D_e values derived for the SAR dataset using (1) the SAR DRCs and (2) the SGCs were compared and consistent results were returned with ratios of between 0.97 ± 0.14 and 1.12 ± 0.14 for all but two samples. IDD1-1 yielded a ratio of 0.95 ± 0.30 and SHAC2 yielded a ratio of 1.30 ± 0.19, for which are both triggered by one extreme outlier. The general performance of the SGC is good, and hence its use was justified.

RESULTS

D_e distributions

For all but one site (SHAC), which will be presented separately below, three types of D_e distributions were observed and representative examples are shown in Figure 7 (all plots in Supplementary Figure 1). Type 1 distributions are characterized by low-degree positive skew and overdispersion (OD) values ≤ 4%. Only a few outliers are observed at the upper and/or lower end of the distributions (Fig. 7). Most samples, aeolian and fluvial, fall into this group (FDU, KAD, AQP, IDD2), and CAM D_e values range between 21 ± 1 Gy (IDD2A) and 89 ± 3 Gy (AQP5; Table 2). Importantly, all three samples of FDU, which are expectedly well-bleached dune samples, present Type 1 distributions. MAM D_e values were calculated to assess whether a positive skew affects the D_e
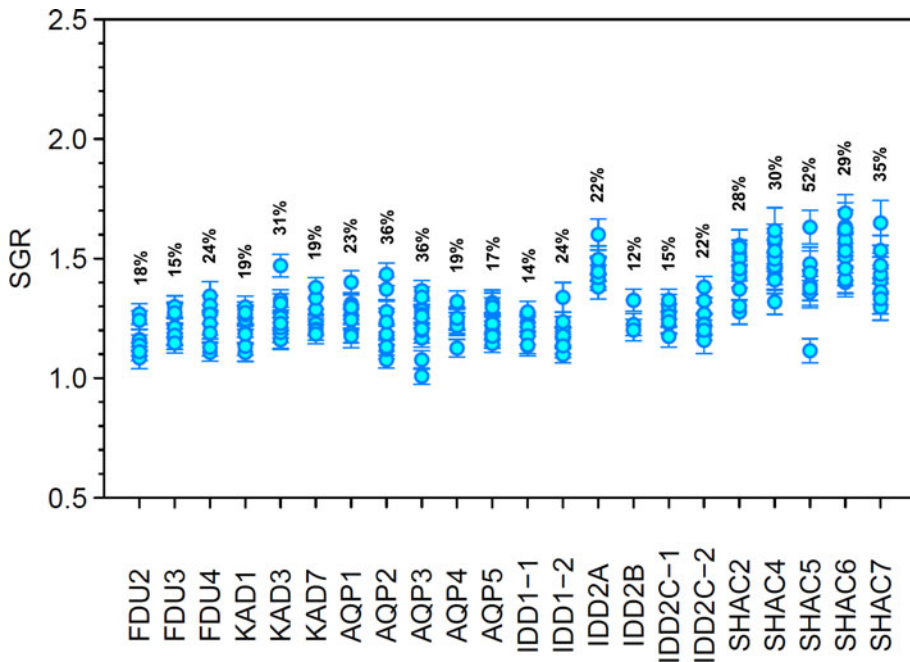
Figure 5. Signal Growth Ratios (SGRs) for all measured full SAR measurements derived using the two highest regenerative dose points. The percentage of spread is given for each sample. SGRs are mainly consistent with each other, indicating that the dose response curves (DRCs) obtained for each sample have similar shapes.
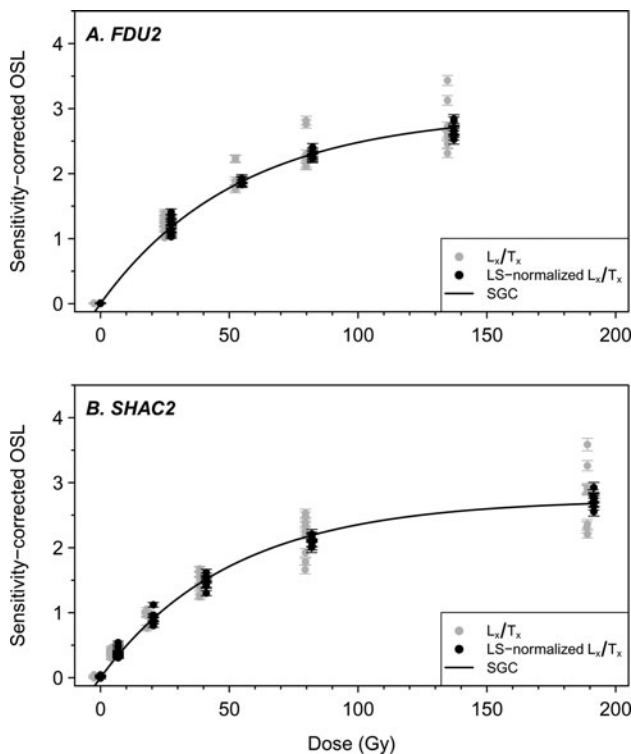

Figure 6. Two representative examples of regenerative dose points of the full SAR measurements before and after LS-normalization. The latter is used to derive the SGCs.

value determination; however, MAM D_e values are consistent with those derived using the CAM. This indicates that outliers on either end of the populations have little influence on final D_e values. Also, similar D_e distribution shapes of well-bleached aeolian samples (FDU) and fluvial samples (KAD, AQP1–AQP4, IDD2) point towards sufficient bleaching during fluvial transport and that derived D_e values represent post-depositional trapped charge.

One distribution (IDD1-1), Type 2, is best described by a wide spread of D_e values, an OD value of $\geq 48\%$, and no obvious separate distribution is present (Fig. 7). In the absence of post-depositional disturbances, such a spread is likely caused by incomplete bleaching during transport. Therefore, only the lower part of the distribution may represent post-depositional trapped charge, and consequently only a MAM D_e value of 24 ± 3 Gy will describe an appropriate dose for this sample.

Another sample (IDD1-2) is characterized by a rather small OD value of 13 ± 4% and truncation because a number of aliquots were rejected due to being in saturation (Supplementary Table 9; Fig. 7). For this Type (3), a CAM D_e value of $\geq 104 \pm 4$ Gy (IDD1-2) was derived. This D_e value has to be regarded as a minimum estimate because only the lower, constrainable D_e values are used to derive the average.

For SHAC, D_e distributions are presented in Figure 8. Distributions of SHAC4, 5, and 7 are characterized by a very wide spread of D_e values and OD values between 64 ± 7% and 118 ± 13% (Table 2). These samples likely suffer from partial bleaching and are most similar to the Type 2 distribution. MAM D_e values of 16.3 ± 2.2 (SHAC4), 3.7 ± 0.8 (SHAC5), and 1.8 ± 0.4 Gy (SHAC7) were calculated. All other SHAC samples are characterized by truncated distributions with many (9–32) aliquots of these samples in saturation (Supplementary Table 9). SHAC2 is characterized by a D_e distribution similar to IDD1-2 (Type 3) with a much lower OD value of 24 ± 5%. A CAM minimum D_e estimate of $\geq 101 \pm 7$ Gy and MAM D_e value of 86 ± 11 Gy were calculated. For SHAC6, no distinct population at the lower end of the D_e distribution is reported. A CAM minimum D_e estimate of $\geq 92 \pm 8$ Gy and MAM D_e values of 41 ± 5 Gy were derived.

Dose rates and age calculations

For most samples, a DR of between 0.96 ± 0.07 (SHAC2) and 1.25 ± 0.11 Gy/ka (IDD1-1) was determined. Only the DR of the proximal gravelly samples KAD1, 3, and 7 are much lower with values

Table 2. D_e determination data for all samples. n_{acc}/n_{meas} = number of accepted and totally measured aliquots; DR = dose rate; OD = overdispersion. D_e values and ages accepted for geochronological consideration are presented in bold. # Samples with truncated distributions for which CAM D_e values and ages are considered to be minimum estimates.

Sample code	Grain size (μm)	n_{acc}/n_{meas}	DR_{total} (Gy/ka)	OD (%)	D_{e_CAM} (Gy)	D_{e_MAM} (Gy)	Age_CAM (ka)	Age_MAM (ka)
FDU2	150–200	40/40	1.02 ± 0.05	17 ± 2	**37.6 ± 1.0**	37.6 ± 1.9	**37.0 ± 2.0**	37.0 ± 2.6
FDU3	150–200	42/43	1.12 ± 0.07	16 ± 2	**45.5 ± 1.0**	45.5 ± 2.4	**40.8 ± 2.6**	40.8 ± 3.2
FDU4	150–200	38/38	1.19 ± 0.06	16 ± 2	**48.3 ± 1.3**	48.3 ± 2.7	**40.5 ± 2.1**	40.5 ± 2.9
KAD1	100–150	43/43	0.35 ± 0.02	18 ± 2	**55.5 ± 1.6**	54.8 ± 3.3	**160.5 ± 7.9**	158.5 ± 11.4
KAD3	100–150	41/42	0.33 ± 0.02	22 ± 3	**48.9 ± 1.7**	47.0 ± 3.0	**148.7 ± 8.2**	142.9 ± 11.0
KAD7	100–150	39/41	0.44 ± 0.03	20 ± 2	**59.5 ± 2.0**	58.2 ± 4.0	**134.4 ± 8.1**	131.5 ± 11.2
AQP1	150–200	42/42	1.23 ± 0.07	22 ± 3	**42.0 ± 1.5**	42.0 ± 2.0	**34.1 ± 1.9**	34.1 ± 2.1
AQP2	150–200	43/43	1.22 ± 0.08	18 ± 2	**48.1 ± 1.4**	47.3 ± 2.6	**39.4 ± 2.5**	38.7 ± 3.0
AQP3	150–200	42/43	1.26 ± 0.06	15 ± 2	**50.5 ± 1.2**	50.3 ± 2.7	**40.2 ± 1.9**	40.1 ± 2.7
AQP4	150–200	40/40	1.11 ± 0.05	14 ± 2	**47.7 ± 1.1**	47.7 ± 2.4	**43.0 ± 2.1**	43.0 ± 2.8
AQP5	150–200	40/43	1.17 ± 0.08	18 ± 2	**89.1 ± 2.8**	88.2 ± 6.1	**76.3 ± 5.3**	75.6 ± 7.0
IDD1-1	150–200	37/40	1.25 ± 0.11	49 ± 6	45.4 ± 3.6	**23.7 ± 2.8**	36.3 ± 3.3	**18.9 ± 2.4**
IDD1-2	150–200	17/50#	1.25 ± 0.09	13 ± 4	**≥104.3 ± 4.3#**	106.4 ± 9.4	**≥83.2 ± 5.9#**	84.9 ± 9.0
IDD2A	150–200	42/42	1.23 ± 0.07	17 ± 2	**21.0 ± 0.6**	21.0 ± 1.1	**17.0 ± 1.0**	17.0 ± 1.2
IDD2B	150–200	39/39	1.12 ± 0.07	24 ± 3	**24.8 ± 1.0**	23.6 ± 0.8	**20.0 ± 1.2**	19.4 ± 1.1
IDD2C-1	150–200	40/40	1.12 ± 0.06	17 ± 2	**21.9 ± 0.6**	21.6 ± 1.2	**19.5 ± 1.1**	19.3 ± 1.4
IDD2C-2	150–200	42/43	1.28 ± 0.07	22 ± 3	**25.1 ± 0.9**	—	**19.6 ± 1.0**	—
SHAC2	100–150	20/54#	0.96 ± 0.07	25 ± 5	**≥101.3 ± 6.5#**	86.2 ± 11.3	**≥105.8 ± 8.2#**	90.0 ± 12.4
SHAC4	100–150	39/46#	1.03 ± 0.12	64 ± 7	≥47.7 ± 4.9#	**16.3 ± 2.2**	≥46.3 ± 5.2#	**15.8 ± 2.3**
SHAC5	100–150	39/42	1.07 ± 0.17	89 ± 10	13.4 ± 1.9	**3.7 ± 0.8**	12.5 ± 1.9	**3.5 ± 0.8**
SHAC6	100–150	38/46#	1.12 ± 0.10	50 ± 6	≥91.9 ± 7.5#	**40.6 ± 5.2**	≥82.1 ± 7.4#	**36.3 ± 4.8**
SHAC7	100–150	41/43	1.13 ± 0.22	118 ± 13	7.9 ± 1.5	**1.8 ± 0.4**	7.0 ± 1.4	**1.6 ± 0.4**

between 0.33 ± 0.02 (KAD3) and 0.44 ± 0.03 Gy/ka (KAD7) (Supplementary Table 10).

For the dune site FDU, consistent (1σ) ages of 37 ± 2 (FDU2), 41 ± 3 (FDU3), and 41 ± 2 ka (FDU4) were obtained (Fig. 2). At the gravel pit of KAD, ages increase with depth from 134 ± 8 (KAD7) to 161 ± 8 ka (KAD1). Similarly, the fluvial sequence of AQP (AQP1–4), is dated to between 34 ± 2 (AQP1) to 43 ± 2 ka (AQP4), increasing with depth. These fluvial units are underlain by an aeolian sand unit of 76 ± 5 ka (AQP5).

All samples of fluvial origin along the IDD sections present consistent (1σ) ages of 20 ± 1 ka (IDD2C-1, IDD2C-2) and 19 ± 2 ka (IDD1-1). The latter is underlain by a much older aeolian unit (Fig. 2) that yielded a minimum age estimate of ≥83 ± 6 ka (IDD1-2). Ages of 20 ± 1 (IDD2B) and 17 ± 1 ka (IDD2A) were obtained for two additional aeolian units.

All five SHAC samples presented complex D_e distributions (see further discussion below in subsection "Luminescence chronology"). Minimum age estimates of ≥106 ± 8, ≥46 ± 5, ≥82 ± 7 ka (CAM), and MAM ages of 90 ± 12, 16 ± 2, and 36 ± 5 ka were obtained for samples from cemented units SHAC2, SHAC4, and SHAC6, respectively. For intervening units, ages of 3.5 ± 0.8 (SHAC5) and 1.6 ± 0.4 ka (SHAC7) were derived.

DISCUSSION

Luminescence chronology

OSL signal properties were assessed for the investigated samples and found to be suitable for dating (see subsection

Table 3. SGC performance measurements.

Sample Code	FOM	Average Error	SGC vs SAR D_{e_CAM} ratio
FDU2	3.9	0.01	0.98 ± 0.08
FDU3	4.6	0.01	0.97 ± 0.04
FDU4	4.3	0.02	0.98 ± 0.10
KAD1	3.6	0.01	1.00 ± 0.07
KAD3	5.9	0.02	0.97 ± 0.14
KAD7	4.9	0.02	0.98 ± 0.11
AQP1	3.8	0.01	1.00 ± 0.08
AQP2	5.9	0.02	0.99 ± 0.08
AQP3	6.9	0.02	0.97 ± 0.09
AQP4	3.0	0.01	1.00 ± 0.07
AQP5	4.4	0.01	1.05 ± 0.10
IDD1-1	3.0	0.01	0.95 ± 0.30
IDD1-2	4.2	0.01	1.12 ± 0.14
IDD2A	4.9	0.01	1.01 ± 0.08
IDD2B	3.8	0.01	0.99 ± 0.05
IDD2C-1	3.2	0.01	0.98 ± 0.03
IDD2C-2	4.9	0.01	0.98 ± 0.09
SHAC2	4.8	0.01	1.30 ± 0.19*
SHAC4	7.0	0.01	1.09 ± 0.32
SHAC5	9.0	0.02	1.07 ± 0.43
SHAC6	7.7	0.01	1.04 ± 0.30
SHAC7	5.1	0.01	1.02 ± 0.62

* one extreme outlier.

"Luminescence properties and performance"). SAR measurement protocol performance was ensured and the applicability of the SGC approach was confirmed. Obtained D_e distributions (see subsection "D_e distributions") were assessed for partial bleaching with most samples showing distributions and OD values similar to those of the expectedly well-bleached dune sands (Type 1). While for those samples average D_e values were calculated using a CAM, for one sample (IDD1-1; Type 2) partial bleaching was indicated by its D_e distribution and a MAM D_e value was obtained. However, the calculated age of the latter is consistent with CAM ages obtained for most other samples from this site (Table 2). Another sample (IDD1-2) has been shown to be at the saturation limit represented by truncated distribution (Type 3) and only a minimum age estimate was yielded using the CAM. Together with the overall consistent estimates, this gives confidence in the reported ages for all investigated sites with the exception of SHAC.

For the lowermost sample, SHAC2, the age represents a minimum estimate because it is derived from a truncated D_e distribution (Type 3), hampering assessment of partial bleaching in this particular case. This indicates that fluvial activity occurred at or prior to 106 ± 8 ka, but prohibits any further chronological conclusions. All other samples from the SHAC site show clear evidence for partial bleaching (high OD and pronounced positive skewness). Samples SHAC4, 5, and 7 show D_e distributions

with a distinct population at the lower edge similar to those reported for most of the other fluvial samples of this study, which gives some confidence that these represent the fully bleached population of grains at the time of deposition (Fig. 8). In contrast, SHAC6 shows a tail of D_e values at the lower end of the distribution. We speculate that in this case, all D_e values represent partially bleached signals and the main population ~90 Gy might represent the original dose of the sediment prior to redeposition. This value is similar to that of the basal sample (SHAC2) and suggests that any age calculated for sample SHAC6 should be considered unreliable. Therefore, SHAC6 has been rejected for chronological interpretation. When applying the MAM to the remaining three samples, the dataset for this site is internally chronologically consistent. Accordingly, the lower part represents different phases of deposition during the Late Pleistocene, whereas the upper part of the sequence falls into the Late Holocene.

Implications for fluvial dynamics in SE Arabia

The OSL ages reported here for fluvial deposition mainly fall within three periods of time (Table 2; Figs. 2, 9). The first cluster has been determined for the coarse proximal gravel deposits from the Khadra Quarry (KAD) and falls into the second half of MIS 6 (Fig. 9); considering age uncertainties, the upper part of the sequence also could correspond to MIS 5e. In fact, deposition of 11 m of sediment at this site apparently comprises several thousand years, if not some tens of thousands of years (ca. 160–135 ka). The second time period of aggradation is represented by a cluster of ages that is observed at two sites, Faya Dune (FDU) and Aqabah Pylon (AQP), and represents deposition ca. 40–35 ka. Interestingly, these two sites represent quite different modes of deposition; aeolian (FDU) and fluvial (AQP), respectively. The third cluster of ages, found for the different sites along Wadi Iddayyah (IDD), is ca. 20 ka. Again, this includes both aeolian and fluvial deposits. Finally, there is evidence for fluvial deposition during the final parts of both the Pleistocene and Holocene, but without a clear clustering of ages.

The most striking and unexpected observation is the fact that OSL ages reported here do not occur during identified eccentricity-modulated interglacial periods, but rather fall into phases of insolation driven, orbital scale increases in rainfall reported in the literature (Parton et al., 2015b) based on phases of speleothem growth at Hoti and Qunf caves, Oman and Mukalla, Yemen, respectively (Burns et al., 2001; Fleitmann et al., 2003, 2011; Nicholson et al., 2020) and lake formation (Parker, 2010; Parton et al., 2018; Groucutt et al., 2021). In addition, there appears to be only a loose correspondence between the timing of fluvial deposition and the monsoon index peaks (MIP) suggested as a reference system by Bretzke et al. (2022) (Fig. 9). In the following, the OSL ages reported here are discussed in the context of the existing regional chronology.

The 11 m thick sequence Khadra (KAD) comprises in its basal part (Fig. 2; Supplementary Table 3, Unit 1) coarse, very poorly sorted, clast-supported gravel with imbricated cobbles and boulders up to 30–55 cm in size. These were deposited under high energy conditions. Unit 1 was dated to 161 ± 8 ka (KAD1), placing the onset of accumulation into late MIS 6, while Unit 1 B shows a fining-upwards sequence. The main sequence represents a series of channel fills with multiple fining-upwards sequences. Unit 3 is represented by alternating layers of fine, planar-bedded ophiolite gravels and sands dated to 149 ± 8 ka (KAD3). These are
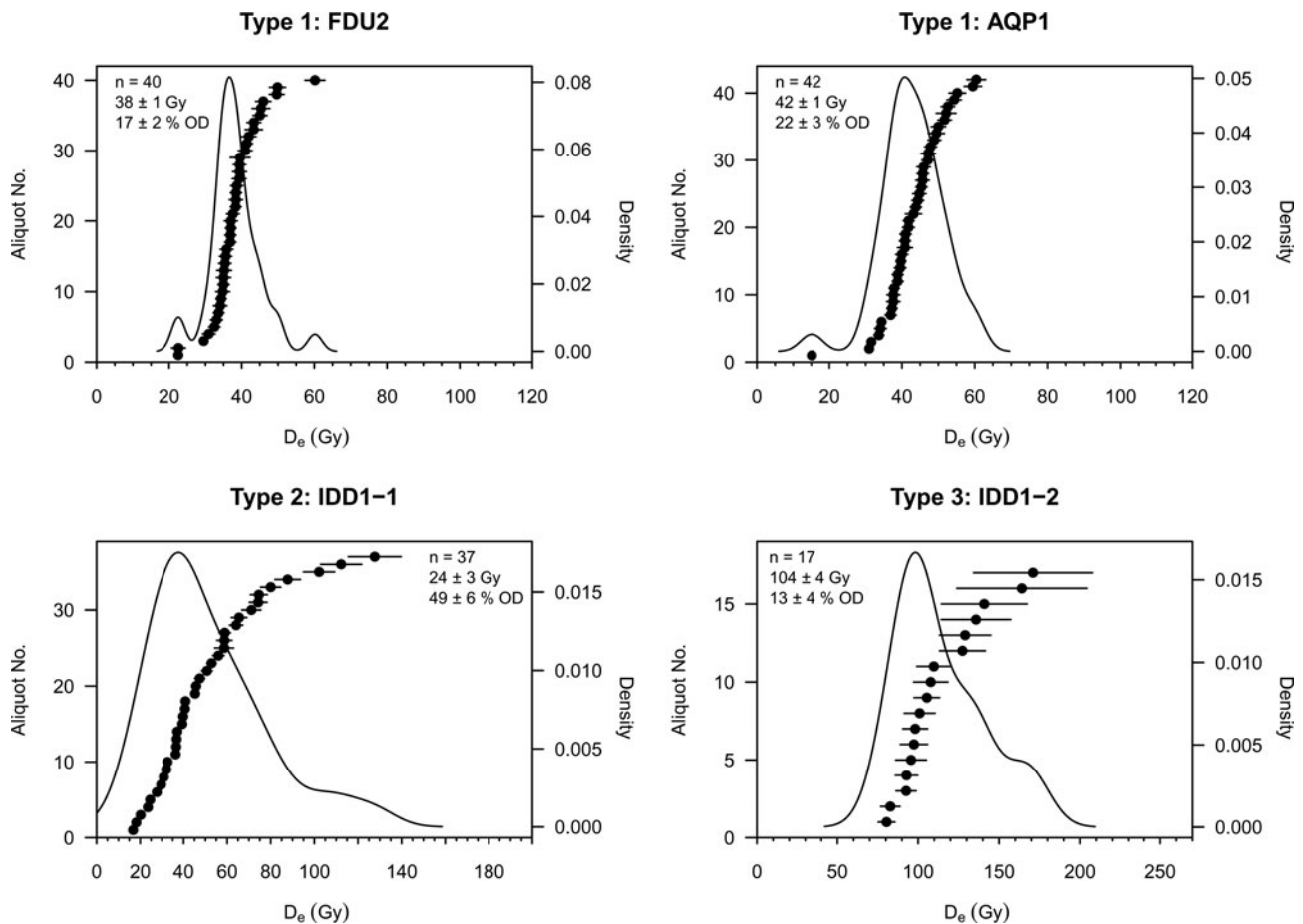
Figure 7. Representative D_e distributions. Type 1 distributions were observed for all aeolian samples (FDU) and only some fluvial deposits (e.g., AQP1), while the other fluvial samples were of Type 2 and 3. Number of accepted measurements (n), CAM D_e, and overdispersion (OD) values are given for all samples except IDD1-1. For the latter, the denoted D_e value was derived using the MAM.

overlain by a high energy flood deposit (Unit 4) denoted by clast-supported cobbles and gravels with some imbrication. The upper part of the sequence (Units 5 and 6) comprises up to ten fining-upwards sequences with the uppermost dated to 134 ± 8 ka (KAD7).

The KAD record coincides with alluvial fan activation at Sibetah, 90 km to the south, also located at the foot of the Hajar Mountains. There, 20 m of fluvial and alluvial sediments were deposited (ca. 160–150 ka) due to activation of the drainage system during which conditions were wet enough for development of savannah-type grasslands with a woody component (Parton et al., 2015b). Both of these records span a precessionally driven insolation peak within MIS 6 (MIP13) at ca. 150 ka (Fig. 9) (Bretzke et al., 2022).

In addition, fluvial silts and gravels, dated from Wadi Dhaid 45 km downstream from Khadra, correspond to fluvial discharge reaching the medial to distal end of the catchment during MIS 6 at 174 ± 24 and 152 ± 14 ka, respectively (Parker and Rose, 2008). Interdunal lacustrine/wetland deposits also have been dated farther inland, in the Rub' al-Khali desert interior, from Liwa (160 ± 8 ka), from fluvio-lacustrine sediments (147 ± 12 ka) in the Sabkha Matti (Goodall, 1995), and from lacustrine silts at Khujaymah, in the Rub' al-Khali from Saudi Arabia at 147 ± 15 ka (Rosenberg et al., 2011).

Although evidence for increased rainfall during MIS 6 has been reported from speleothems from the Levant, central Negev, and southern Jordan (Bar-Matthews et al., 2003; Vaks et al., 2010), this has not been shown from southern Arabian cave records (Fleitmann et al., 2011). Based on the lack of dated speleothems, it has been suggested that the region was under a continually hyper-arid climate during MIS 6, with monsoon rainfall displaced substantially south due to increased glacial boundary conditions (Fleitmann et al., 2011). Interestingly, the middle of MIS 6 coincides with MIP 13, and incipient soil formation at this time has been reported at al-Mamla on the southwestern edge of the Wahiba Sands between ca. 160–140 ka (Preusser et al., 2002; Radies et al., 2004). Significantly, this period also coincides with occupation recorded at Jebel Faya, indicating that widespread ephemeral drainage activation during MIS 6 was sufficient to support early human populations in SE Arabia, despite an absence of supporting evidence from lacustrine and speleothem records (Bretzke et al., 2022). However, the overall picture of changing rainfall levels during MIS 6 remains poorly understood to this point.

Although not shown in the new ages presented here, evidence for active alluvial and fluvial deposition during MIS 5 corresponding with insolation maxima has been demonstrated from a number of sites across SE Arabia. At Al Ain (Atkinson et al., 2013) and
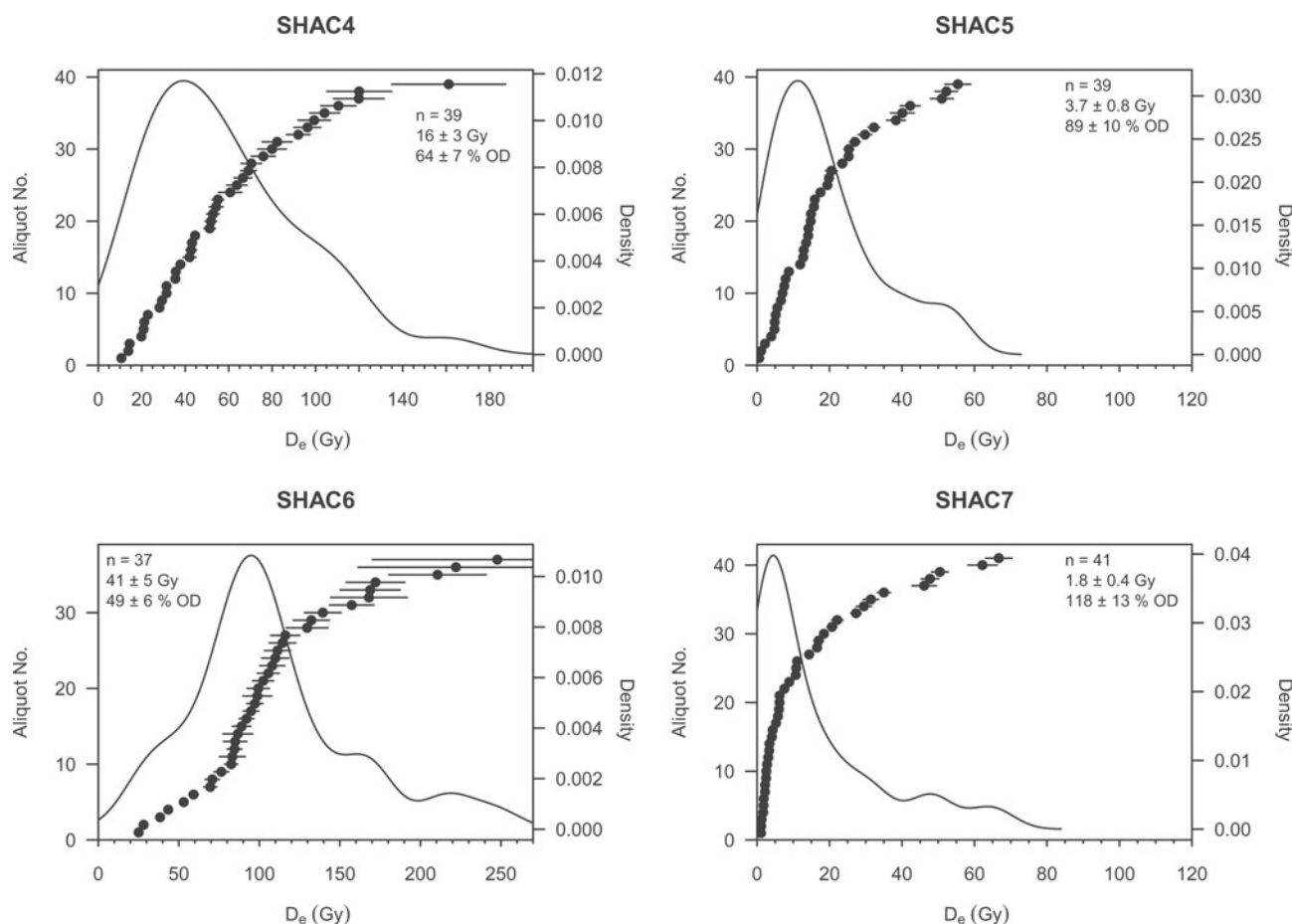
Figure 8. D_e distributions of samples from the site SHAC. Number of accepted measurements (n), MAM D_e, and CAM overdispersion (OD) values are given.

Sibetah (Parton et al., 2015b), thick sequences of alluvial and fluvial sediments were deposited in MIS 5e (135–115 ka) and MIS 5a (90–76 ka). Within the study area, perennial channel flow was demonstrated at Tawi Asmar, in the medial to distal end of Wadi Dhaid (Atkinson et al., 2013), where a >20 m thick meandering channel filled with gravels and sands was dated to 115–76 ka (MIS 5c–5a). Hili Formation fluvial gravels from a relict paleodrainage system, stretching over a distance of ∼150 km from the Hajar Mountains near Al Ain to Abu Dhabi, also have been dated to between 133–77 ka (Farrant et al., 2012, 2015). In Oman, at the distal end of an alluvial fan drainage network from the Jebel Ahkdar region, paleolake sediments from Saiwan were dated between 132–104 ka (Rosenberg et al., 2012). These phases of fluvial activation and channel flow correspond to speleothem formation in Oman and Yemen during MIS 5, indicating rainfall in excess of 350 mm/yr (Burns et al., 2001; Fleitmann et al., 2003). While evidence for enhanced fluvial activity for this period has not been found in the current study, this most likely is linked to the availability of sediment exposures and sampling strategy.

Across the region, MIS 4 has been suggested as arid. At the transition between late MIS 5 and the onset of MIS 4, aeolian sands dated at AQP5 (76 ± 5 ka; current study) agree well with those found at Sibetah (73 ± 7 ka) (Parton et al., 2015b). Also, farther to the west, in the western region of Abu Dhabi in the Rub' al Khali, aeolian sands from both the coastal region carbonate-rich Ghayathi Formation and the red quartz-rich sands of the Madinat Zayed Formation were dated to ca. 78–70 ka (Farrant et al., 2012, 2015). Within the Liwa region of the UAE, foreset dune sands were dated to 71 ± 5 ka (Wood et al., 2003).

Evidence for a period of increased wetness, congruent with a precessionally paced insolation maxima (MIP 5), has been suggested based on data from the Wadi Iddayyah catchment area, by dating of lacustrine deposits and flood silts at Jebel Aqabah (61–58 ka; Parton et al., 2013). Farther to the south, redevelopment of a braided channel network during a subsequent phase was identified in distal exposures of the Al Sibetah fan at Remah, ∼50 km southwest of the Hajar Mountains, dating to 67–61 ka and ca. 55 ka (Farrant et al., 2012). These ages are corroborated by interdunal wetland deposits from the Liwa region of the Rub' al Khali, dated to 64 ± 6 and 54 ± 4 ka, which corresponds to the same time interval (Wood et al., 2003). In Wadi Mistal, Oman, Hoffmann et al. (2015) dated a suite of fine-grained playa-like sediments that formed behind a landslide-dammed ephemeral lake between ca. 57–43 ka. During this time, rather than continuous rainfall under a monsoonal regime, the authors proposed multiple strong, short-lived precipitation events. Farther south in Oman, evidence for activation of the distal part of the drainage network is recorded from alluvial fan deposits dated to 45 ± 5 ka (Blechschmidt et al., 2009).

For the late MIS 3 stage, our results show a complex interplay between aeolian and fluvial process. Within the catchment study area, at FDU, 4 m of dune sands were emplaced between 41–37 ka, preserving evidence for rainfall as several short ponding events with desiccation curls occurring towards the base of the sequence.
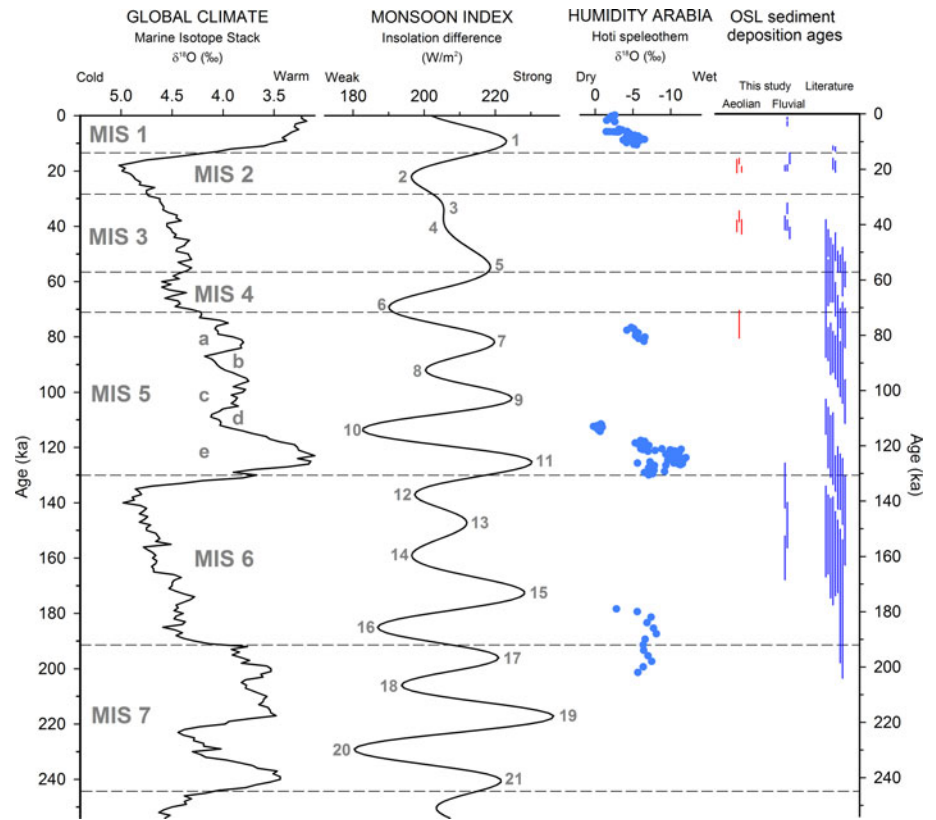
Figure 9. Summary figure displaying fluvial sediment OSL deposition ages determined within the present study and those reported in the literature (Krbetschek et al., 2008; Parker and Rose, 2008; Atkinson et al., 2012, 2013; Farrant et al., 2012, 2015; Parton et al., 2013, 2015b; Hoffmann et al., 2015) for SE Arabia. Additionally, ages for aeolian deposits determined in the present study are displayed. The Marine Isotope Stack of Lisiecki and Raymo (2005) is shown as a measure of global climate conditions. The Monsoon Index (Leuschner and Sirocko, 2003) is given as an expression of potential theoretical climate forcing.

At AQP, located 1 km south of the fluvio-lacustrine silts studied by Parton et al. (2013), multiple fining-upwards sequences of fluvial sands and silts are dated between 43–34 ka (APQ4 to 1). Deposition of Unit 2 at AQP (Fig. 2) is linked to repeated phases of channel flow that led to the accumulation of fluvially deposited silts and planar-bedded sands that fine upwards into carbonate-rich sands, each indicating a gradual waning of stream flow and desiccation. At least four cycles of these aggradation phases are recorded in this unit. At the present time, it is not possible to determine whether these phases represent a series of strong, short-term precipitation events or a more-pronounced humid phase because three of the OSL ages at AQP overlap, potentially suggesting very rapid deposition. However, the OSL ages determined for the AQP fluvial sequence are close to the age calculated for a weak precessionally driven insolation maxima, corresponding with MIP 3 (Fig. 9).

Most paleoclimate evidence suggests that hyper-arid conditions prevailed throughout much of MIS 2, during which there was widespread dune mobilization and emplacement throughout SE Arabia (Goudie et al., 2000; Parker and Goudie, 2008; Leighton et al., 2014; Farrant et al., 2015). The main phase of dune accumulation occurred between 22–20 and 16–9 ka, respectively, and has been attributed to both high sediment availability and wind-driven transport capacity (Preusser et al., 2002; Preusser, 2009; Thomas and Bailey, 2019). In Wadi Iddayyah, the complex interplay between aeolian and fluvial processes is also shown at ca. 20 ka by the current study. The accumulation of several distinct silt units in the medial to distal wadi at IDD1 and IDD2 implies that there was sufficient rainfall to generate low-energy channel flow or standing water during MIS 2 (ca. 20 ka), although the stability and duration of these phases remain unclear. This concurs well with fluvial sediments dated to 19 ± 2 and 18 ± 2 ka at paleolake

Saiwan in Oman, located at the distal end of the alluvial fan drainage network (Rosenberg et al., 2012). Along with similarly dated travertine deposition at Nizwa (Clark and Fontes, 1990), this implies some water availability at this time.

The three reliable OSL ages for the Sharjah Army Camp (SHAC) point towards episodic fluvial deposition in this distal part of the drainage network (at 16 ± 2, 3.5 ± 0.8, and 1.6 ± 0.4 ka). It should be noted that these likely do not record all phases of deposition at this site. Furthermore, it is interesting to recognize that so far no fluvial deposition has been dated for the pronounced humid period that occurred during early MIS 1 (ca. 11–6 ka). This suggests either no accumulation occurred during this time, or these sediments have not been preserved, or sediments falling into this period have not been sampled yet. The latter could be explained by the fact that these young sediments might be deeply buried and are not easily accessible. Indeed, the widespread evidence for lake formation and speleothem growth during the Early Holocene would appear to support this supposition.

CONCLUSIONS

Fluvial systems offer considerable potential to address the current gaps in knowledge that exist in understanding of late Quaternary environmental change in Arabia, with evidence from some key periods limited to just a handful of spatially dispersed, terrestrial records. The new OSL ages reported here for proximal to distal fluvial systems in SE Arabia fall into three main periods of fluvial activity of the drainage networks: 160–135 (MIS 6), 43–34 (MIS 3), and ca. 20 ka (MIS 2). These ages, as well as single ages determined for the Late Pleistocene and Late Holocene, all fall outside of previously proposed major wet periods from Arabia.

Alluvial fan and fluvial activation during MIS 6 could correspond with precessionally driven insolation and monsoon-driven maxima outside of global interglacials. The complex interplay between fluvial and aeolian dynamics is recorded during late MIS 3, with evidence for drainage activation and episodic channel flow ca. 43–34 ka (AQP), as well as aeolian dune accumulation ca. 41–37 ka (FDU). This is perhaps unsurprising given that relatively short-lived ephemeral drainage activation during MIS 3 would have occurred alongside dune accretion within a predominantly arid environment. Evidence from the late MIS 3 nonetheless corresponds to a period of weak insolation maxima. Sufficient rainfall to generate channel flow/standing water is also reported during MIS 2 (ca. 20 ka), thereby suggesting that the hyper-arid conditions that are widely thought to have prevailed throughout much of MIS 2 were punctuated by possibly short-lived periods of increased rainfall or possibly even phases of centuries to millennia.

The data presented here show that the eccentricity-timed insolation changes, as previously reported from lake (Groucutt et al., 2021) and speleothem records elsewhere in Arabia (Fleitmann et al., 2011), cannot alone account for the internal complexity of fluvial systems within the region. Such complexity is likely driven by a range of endogenic and exogenic factors, such as regional topography, underlying geological formations, and base-level changes, alongside regional synoptic climate variability. Future work will need to produce much larger data sets from a range of environments to decipher if certain peaks can be identified clearly and directly attributable to orbital forcing parameters. Furthermore, the occurrence of fluvial accumulation during periods of supposed hyper-aridity challenges a longstanding wet/dry dichotomy in Arabia, while simultaneously enhancing the debate regarding early human occupation of arid regions.

Supplementary Material. The supplementary material for this article can be found at https://doi.org/10.1017/qua.2022.51

REFERENCES

Abrams, M.J., Chadwick, O.H., 1994. Tectonic and climatic implications of alluvial fan sequences along the Batinah coast, Oman. *Journal of the Geological Society* 151, 51–58.

Al Farraj, A., Harvey, A.M., 2000. Desert pavement characteristics on wadi terrace and alluvial fan surfaces: Wadi Al-Bih, U.A.E. and Oman. *Geomorphology* 35, 279–297.

Al Farraj, A., Harvey, A.M., 2004. Late Quaternary interactions between aeolian and fluvial processes: a case study in the northern UAE. *Journal of Arid Environments* 56, 235–248.

Al Farraj, A., Harvey, A.M., 2005. Morphometry and depositional style of Late Pleistocene alluvial fans: Wadi Al-Bih, northern UAE and Oman. *Geological Society, London, Special Publications* 251, 85–94.

Anderson, J.M., 2007. *Climatic and Structural Controls on the Geomorphology of Wadi San, Highland Southern Yemen.* MSc Thesis, University of South Florida, Tampa, Florida, 52 pp.

Armitage, S.J., Jasim, S.A., Marks, A.E., Parker, A.G., Usik, V.I., Uerpmann, H.P., 2011. The southern route "out of Africa": evidence for an early expansion of modern humans into Arabia. *Science* 331, 453–456.

Atkinson, O.A., Thomas, D.S., Goudie, A.S., Parker, A.G., 2012. Holocene development of multiple dune generations in the northeast Rub' al-Khali, United Arab Emirates. *The Holocene* 22, 179–189.

Atkinson, O.A., Thomas, D.S., Parker, A.G., Goudie, A.S., 2013. Late Quaternary humidity and aridity dynamics in the northeast Rub' al-Khali, United Arab Emirates: implications for early human dispersal and occupation of eastern Arabia. *Quaternary International* 300, 292–301.

Bailey, R.M., 2000. The interpretation of quartz optically stimulated luminescence equivalent dose versus time plots. *Radiation Measurements* 32, 129–140.

Bar-Matthews, M., Ayalon, A., Gilmour, M., Matthews, A., Hawkesworth, C.J., 2003. Sea-land oxygen isotopic relationships from planktonic foraminifera and speleothems in the Eastern Mediterranean region and their implication for paleorainfall during interglacial intervals. *Geochimica et Cosmochimica Acta* 67, 3181–3199.

Besler, H., 1982. The north-eastern Rub-Al Khali within the borders if the United Arab Emirates. *Zeitschrift für Geomorphologie NF* 26, 495–504.

Blechschmidt, I., Matter, A., Preusser, F., Rieke-Zapp, D., 2009. Monsoon triggered formation of Quaternary alluvial megafans in the interior of Oman. *Geomorphology* 110, 128–139.

Bretzke, K., Preusser, F., Jasim, S., Miller, C., Preston, G., Raith, K., Underdown, S.J., Parton, A., Parker, A.G., 2022. Multiple phases of human dispersal into Arabia between 210,000 and 120,000 years ago. *Scientific Reports* 12, 1600. https://doi.org/10.1038/s41598-022-05617-w.

Burns, S.J., Fleitmann, D., Matter, A., Neff, U., Mangini, A., 2001. Speleothem evidence from Oman for continental pluvial events during interglacial periods. *Geology* 29, 623–626.

Burns, S.J., Matter, A., Frank, N., Mangini, A., 1998. Speleothem-based paleoclimate record from northern Oman. *Geology* 26, 499–502.

Burow, C., 2020a. calc_CentralDose(): Apply the central age model (CAM) after Galbraith et al. (1999) to a given D_e distribution. Function version 1.4.0. In: Kreutzer, S., Burow, C., Dietze, M., Fuchs, M.C., Schmidt, C., Fischer, M., Friedrich, J., Riedesel, S., Autzen, M., Mittelstrass, D., *Luminescence: Comprehensive Luminescence Dating Data Analysis. R package version 0.9.10.* https://CRAN.R-project.org/package=Luminescence (last accessed: 28/03/2021).

Burow, C., 2020b. calc_MinDose(): Apply the (un-)logged minimum age model (MAM) after Galbraith et al. (1999) to a given D_e distribution. Function version 0.4.4. In: Kreutzer, S., Burow, C., Dietze, M., Fuchs, M.C., Schmidt, C., Fischer, M., Friedrich, J., Riedesel, S., Autzen, M., Mittelstrass, D., *Luminescence: Comprehensive Luminescence Dating Data Analysis. R package version 0.9.10.* https://CRAN.R-project.org/package=Luminescence (last accessed: 28/03/2021).

Clark, I.D., Fontes, J.C., 1990. Paleoclimatic reconstruction in northern Oman based on carbonates from hyperalkaline groundwaters. *Quaternary Research* 33, 320–336.

Clemens, S.C., Prell, W.L., Murray, D., Shimmield, G., Weedon, G., 1991. Forcing mechanisms of the Indian Ocean monsoon. *Nature* 353, 720–725.

Degering, D., Degering, A., 2020. Change is the only constant—time-dependent dose rates in luminescence dating. *Quaternary Geochronology* 58, 101074. https://doi.org/10.1016/j.quageo.2020.101074.

Delagnes, A., Tribolo, C., Bertran, P., Brenet, M., Crassard, R., Jaubert, J., Khalidi, L., et al., 2012. Inland human settlement in southern Arabia 55,000 years ago. New evidence from the Wadi Surdud Middle Paleolithic site complex, western Yemen. *Journal of Human Evolution* 63, 452–474.

Drechsler, P., 2008. Environmental conditions and environmental changes in the Jebel al-Buhais area: the history of an archaeological landscape. In: Uerpmann, H.P., Uerpmann, M., Jasim, S.A. (Eds.), *The Natural Environment of Jebel al-Buhais: Past and Present.* Kerns Verlag, Tübingen, Germany, pp. 17–43.

Edgell, H.S., 2006. *Arabian Deserts: Nature, Origin and Evolution.* Springer Science & Business Media, Dordrecht, The Netherlands.

Engel, M., Matter, A., Parker, A.G., Parton, A., Petraglia, M.D., Preston, G.W., Preusser, F., 2017. Lakes or wetlands? A comment on 'The middle Holocene climatic records from Arabia: reassessing lacustrine environments, shift of ITCZ in Arabian Sea, and impacts of the southwest Indian and African monsoons' by Enzel et al. *Global and Planetary Change* 148, 258–267.

Farrant, A.R., Arkley, S.L.B., Ellison, R.A., Styles, M.T., Phillips, E.R., 2006. *Geology of the Al Dhaid.* 1:100,000 map sheet, 100-2, United Arab Emirates. Keyworth, Nottingham: British Geological Survey, Ministry of Energy, United Arab Emirates.

Farrant, A.R., Duller, G.A., Parker, A.G., Roberts, H.M., Parton, A., Knox, R.W., Bide, T., 2015. Developing a framework of Quaternary dune accumulation in the northern Rub' al-Khali, Arabia. *Quaternary International* 382, 132–144.

Farrant, A.R., Ellison, R.A., Thomas, R.J., Pharaoh, T.C., Newell, A.J., Goodenough, K.M., Lee, J.R., Knox, R.O., 2012. *The Geology and Geophysics of the United Arab Emirates. Volume 6: Geology of the Western and Central United Arab Emirates*. Keyworth, Nottingham: British Geological Survey, Ministry of Energy, United Arab Emirates.

Fisher, M., Membery, D., 1998. Climate. In: Ghazanfar, S.A., Fisher, M. (Eds.), *Vegetation of the Arabian Peninsula, Geobotany*. Kluwer Academic Publishers, Dordrecht, Netherlands, pp. 5–38.

Fleitmann, D., Burns, S.J., Neff, U., Mangini, A., Matter, A., 2003. Changing moisture sources over the last 330,000 years in northern Oman from fluid-inclusion evidence in speleothems. *Quaternary Research* 60, 223–232.

Fleitmann, D., Burns, S.J., Pekala, M., Mangini, A., Al-Subbary, A., Al-Aowah, M., Kramers, J., Matter, A., 2011. Holocene and Pleistocene pluvial periods in Yemen, southern Arabia. *Quaternary Science Reviews* 30, 783–787.

Fleitmann D., Matter, A., 2009. The speleothem record of climate variability in southern Arabia. *Comptes Rendus Geoscience* 341, 633–642.

Fu, X., Li, B., Jacobs, Z., Jankowski, N.R., Cohen, T.J., Roberts R.G., 2020. Establishing standardised growth curves (SGCs) for OSL signals from individual grains of quartz: a continental-scale case study. *Quaternary Geochronology* 60, 101107. https://doi.org/10.1016/j.quageo.2020.101107.

Galbraith, R.F., Roberts, R.G., 2012. Statistical aspects of equivalent dose and error calculation and display in OSL dating: an overview and some recommendations. *Quaternary Geochronology* 11, 1–27.

Galbraith, R.F., Roberts, R.G., Laslett, G.M., Yoshida, H., Olley, J.M., 1999. Optical dating of single and multiple grains of quartz from Jinmium rock shelter, northern Australia: part I, experimental design and statistical models. *Archaeometry* 41, 339–364.

Garzanti, E., Vermeesch, P., Andò, S., Vezzoli, G., Valagussa, M., Allen, K., Kadi, K.A., Al-Juboury, A.I., 2013. Provenance and recycling of Arabian desert sand. *Earth-Science Reviews* 120, 1–19.

Ghazanfar, S.A., 1991. Vegetation structure and phytogeography of Jabal Shams, an arid mountain in Oman. *Journal of Biogeography* 18, 299–309.

Goodall, T.M., 1995. *The Geology and Geomorphology of the Sabkhat Matti Region (United Arab Emirates): A Modern Analogue for Ancient Desert Sediments from North-west Europe*. PhD dissertation, University of Aberdeen, Aberdeen, Scotland, 433 pp.

Goudie, A., 2002. *Great Warm Deserts of the World: Landscapes and Evolution*. Oxford University Press, Oxford, UK.

Goudie, A.S., Colls, A., Stokes, S., Parker, A., White, K., Al-Farraj A., 2000. Latest Pleistocene and Holocene dune construction at the north-eastern edge of the Rub Al Khali, United Arab Emirates. *Sedimentology* 47, 1011–1021.

Groucutt, H.S., White, T.S., Scerri, E.M., Andrieux, E., Clark-Wilson, R., Breeze, P.S., Armitage, S.J., et al., 2021. Multiple hominin dispersals into Southwest Asia over the past 400,000 years. *Nature* 597, 376–380.

Guba, I., Glennie K., 1998. Geology and geomorphology. In: Ghazanfar, S.A., Fisher, M. (Eds.), *Vegetation of the Arabian Peninsula, Geobotany*. Kluwer Academic Publishers, Dordrecht, The Netherlands, pp. 39–62.

Herold, M., Lohmann, G., 2009. Eemian tropical and subtropical African moisture transport: an isotope modelling study. *Climate Dynamics* 33, 1075–1088.

Hoffmann, G., Rupprechter, M., Rahn, M., Preusser, F., 2015. Fluvio-lacustrine deposits reveal precipitation pattern in SE Arabia during early MIS 3. *Quaternary International* 382, 145–153.

Hu, Y., Li, B., Jacobs, Z., 2020. Single-grain quartz OSL characteristics: testing for correlations within and between sites in Asia, Europe and Africa. *Methods and Protocols* 3, 2. https://doi.org/10.3390/mps3010002.

Hu, Y., Marwick, B., Zhang, J.F., Rui, X., Hou, Y.M., Yue, J.P., Chen, W.R., Huang W.W., Li, B., 2019. Late Middle Pleistocene Levallois stone-tool technology in southwest China. *Nature* 563, 82–85.

Jennings, R.P., Singarayer, J., Stone, E.J., Krebs-Kanzow, U., Khon, V., Nisancioglu, K.H., Pfeiffer, M., Zhang, X., et al., 2015. The greening of Arabia: multiple opportunities for human occupation of the Arabian Peninsula during the Late Pleistocene inferred from an ensemble of climate model simulations. *Quaternary International* 382, 181–199.

Krbetschek, M.R., Uerpmann, H.P., Jasim, S.A., 2008. Optically stimulated luminescence (OSL) dating of sediments from Jebel al-Emaylah (UAE). In: Uerpmann, H.P., Uerpmann, M., Jasim, S.A. (Eds.), *The Natural Environment of Jebel al-Buhais: Past and Present*. Kerns Verlag, Tübingen, Germany, pp. 43–45.

Leighton, C.L., Bailey, R.M., Thomas, D.S.G., 2014. Interpreting and modelling late Quaternary dune accumulation in the southern Arabian Peninsula. *Quaternary Science Reviews* 102, 1–13.

Leuschner, D.C., Sirocko, F., 2003. Orbital insolation forcing of the Indian Monsoon—a motor for global climate changes? *Palaeogeography, Palaeoclimatology, Palaeoecology* 197, 83–95.

Li, B., Jacobs, Z., Roberts, R.G., 2016. Investigation of the applicability of standardised growth curves for OSL dating of quartz from Haua Fteah cave, Libya. *Quaternary Geochronology* 35, 1–15.

Li, B., Roberts, R.G., Jacobs, Z., Li, S.H., 2015. Potential of establishing a 'global standardised growth curve' (gSGC) for optical dating of quartz from sediments. *Quaternary Geochronology* 27, 94–104.

Lisiecki, L.E., Raymo, M.E., 2005. A Pliocene–Pleistocene stack of 57 globally distributed benthic $\partial^{18}O$ records. *Paleoceanography* 20, PA1003. https://doi.org/10.1029/2004PA001071.

Macklin, S., Ellison, R.A., Manning, J., Farrant, A.R., Lorenti, L., 2012. Engineering geological characterisation of the Barzaman Formation, with reference to coastal Dubai, UAE. *Bulletin of Engineering Geology and the Environment* 7, 1–19.

Maizels, J.K., 1987. Plio-Pleistocene raised channel systems of the western Sharqiya (Wahiba), Oman. In: Frostick, L.E., Reid, I. (Eds.), Desert Sediments: Ancient and Modern. *Geological Society, London, Special Publications* 35, 31–50.

Maizels, J., McBean, C., 1990. Cenozoic alluvial fan systems of interior Oman: palaeoenvironmental reconstruction based on discrimination of palaeo-channels using remotely sensed data. In: Robertson, A.H.F., Searle, M.P., Reis, A.C. (Eds.), *The Geology and Tectonics of the Oman Region*. Geological Society, London, Special Publications 49, 565–582.

Matter, A., Mahjoub, A., Neubert, E., Preusser, F., Schwalb, A., Szidat, S., Wulf, G., 2016. Reactivation of the Pleistocene trans-Arabian Wadi ad Dawasir fluvial system (Saudi Arabia) during the Holocene humid phase. *Geomorphology* 270, 88–101.

McLaren, S.J., Al-Juaidi, F., Bateman, M.D., Millington A.C., 2009. First evidence for episodic flooding events in the arid interior of central Saudi Arabia over the last 60 ka. *Journal of Quaternary Science* 24, 198–207.

Mueller, D., Preusser, F., 2022. Investigating the applicability of a standardised growth curve approach on Middle Pleistocene sediments from northern Switzerland. *Quaternary Geochronology* 67, 101238. https://doi.org/10.1016/j.quageo.2021.101238.

Murray, A.S., Wintle, A.G., 2000. Luminescence dating of quartz using an improved single-aliquot regenerative-dose protocol. *Radiation Measurements* 32, 57–73.

Nicholson, S.L., Pike, A.W., Hosfield, R., Roberts, N., Sahy, D., Woodhead, J., Cheng, H., et al., 2020. Pluvial periods in Southern Arabia over the last 1.1 million-years. *Quaternary Science Reviews* 229, 106112. https://doi.org/10.1016/j.quascirev.2019.106112.

Pain, C.F., Abdelfattah, M.A., 2015. Landform evolution in the arid northern United Arab Emirates: impacts of tectonics, sea level changes and climate. *Catena* 134, 14–29.

Parker, A.G., 2010. Pleistocene climate change in Arabia: developing a framework for hominin dispersal over the last 350 ka. In: Petraglia, M.D., Rose, J.I. (Eds.), *The Evolution of Human Populations in Arabia, Vertebrate Paleobiology and Paleoanthropology*. Springer, Dordrecht, The Netherlands. pp. 39–49.

Parker, A.G., Eckersley, L., Smith, M.M., Goudie, A.S., Stokes, S., Ward, S., White, K., Hodson, M.J., 2004. Holocene vegetation dynamics in the northeastern Rub' al-Khali desert, Arabian Peninsula: a phytolith, pollen and carbon isotope study. *Journal of Quaternary Science* 19, 665–676.

Parker, A.G., Goudie, A.S., 2008. Geomorphological and palaeoenvironmental investigations in the southeastern Arabian Gulf region and the implication for the archaeology of the region. *Geomorphology* 101, 458–470.

Parker, A.G., Rose, J.I., 2008. Climate change and human origins in southern Arabia. *Proceedings of the Seminar for Arabian Studies* **38**, 25–42.

Parton, A., Clark-Balzan, L., Parker, A.G., Preston, G.W., Sung, W.W., Breeze, P.S., Leng, M.J., *et al.*, 2018. Middle–late Quaternary palaeoclimate variability from lake and wetland deposits in the Nefud Desert, northern Arabia. *Quaternary Science Reviews* **202**, 78–97.

Parton, A., Farrant, A.R., Leng, M.J., Schwenninger, J.L., Rose, J.I., Uerpmann, H.P., Parker, A.G., 2013. An early MIS 3 pluvial phase in southeast Arabia: climatic and archaeological implications. *Quaternary International* **300**, 62–74.

Parton, A., Farrant, A.R., Leng, M.J., Telfer, M.W., Groucutt, H.S., Petraglia, M.D., Parker, A.G., 2015b. Alluvial fan records from southeast Arabia reveal multiple windows for human dispersal. *Geology* **43**, 295–298.

Parton, A., White, T.S., Parker, A.G., Breeze, P.S., Jennings, R., Groucutt, H.S., Petraglia, M.D., 2015a. Orbital-scale climate variability in Arabia as a potential motor for human dispersals. *Quaternary International* **382**, 82–97.

Peng, J., Li, B., 2017. Single-aliquot regenerative-dose (SAR) and standardised growth curve (SGC) equivalent dose determination in a batch model using the R Package 'numOSL'. *Ancient TL* **35**, 32–53.

Peng, J., Li B., More, J., Garbow, B., Hillstrom, K., Burkhardt, J., Gilbert, P., Varadhan, R., 2018. *numOSL: Numeric Routines for Optically Stimulated Luminescence Dating*. R package version 2.6. https://CRAN.R-project.org/package=numOSL (last accessed: 28/03/2021).

Prescott, J.R., Hutton, J.T., 1994. Cosmic ray contribution to dose rates for luminescence and ESR dating: large depths and long-term time variations. *Radiation Measurements* **23**, 497–500.

Preusser, F., 2009. Chronology of the impact of Quaternary climate change on continental environments in the Arabian Peninsula. *Comptes Rendus Geoscience* **341**, 621–632.

Preusser, F., Radies, D., Matter, A., 2002. A 160,000-year record of dune development and atmospheric circulation in southern Arabia. *Science* **296**, 2018–2020.

Radies, D., Preusser, F., Matter, A., Mange, M., 2004. Eustatic and climatic controls on the development of the Wahiba Sand Sea, Sultanate of Oman. *Sedimentology* **51**, 1359–1385.

Richter, D., Richter, A., Dornich, K., 2013. Lexsyg—a new system for luminescence research. *Geochronometria* **40**, 220–228.

Rittenour, T.M., 2008. Luminescence dating of fluvial deposits: applications to geomorphic, palaeoseismic and archaeological research. *Boreas* **37**, 613–635.

Roberts, H.M., Duller, G.A.T., 2004. Standardised growth curves for optical dating of sediment using multiple-grain aliquots. *Radiation Measurements* **38**, 241–252.

Rosenberg, T.M., Preusser, F., Blechschmidt, I., Fleitmann, D., Jagher, R., Matter, A., 2012. Late Pleistocene palaeolake in the interior of Oman: a potential key area for the dispersal of anatomically modern humans out-of-Africa? *Journal of Quaternary Science* **27**, 13–16.

Rosenberg, T.M., Preusser, F., Fleitmann, D., Schwalb, A., Penkman, K., Schmid, T.W., Al-Shanti, M.A., Kadi, K., Matter, A., 2011. Humid periods in southern Arabia: windows of opportunity for modern human dispersal. *Geology* **39**, 1115–1118.

Rosenberg, T.M., Preusser, F., Risberg, J., Plikk, A., Kadi, K.A., Matter, A., Fleitmann, D., 2013. Middle and Late Pleistocene humid periods recorded in palaeolake deposits of the Nafud Desert, Saudi Arabia. *Quaternary Science Reviews* **70**, 109–123.

Thomas, D.S., Bailey, R.M., 2019. Analysis of late Quaternary dunefield development in Asia using the accumulation intensity model. *Aeolian Research* **39**, 33–46.

Thomas, R.J., Schofield, D.I., Goodenough, K.M., Styles, M.T., Farrant, A.R., 2006. *Geology of the Fujairah 1:50 000 map sheet 50-4, United Arab Emirates*. Keyworth, Nottingham: British Geological Survey, Ministry of Energy, United Arab Emirates.

Vaks, A., Bar-Matthews, M., Matthews, A., Ayalon, A., Frumkin, A., 2010. Middle–late Quaternary paleoclimate of northern margins of the Saharan-Arabian Desert: reconstruction from speleothems of Negev Desert, Israel. *Quaternary Science Reviews* **29**, 2647–2662.

Wallinga, J., 2002. Optically stimulated luminescence dating of fluvial deposits: a review. *Boreas* **31**, 303–322.

White, K., Goudie, A., Parker, A., Al-Farraj, A., 2001. Mapping the geochemistry of the northern Rub'Al Khali using multispectral remote sensing techniques. *Earth Surface Processes and Landforms* **26**, 735–748.

Wood, W.W., Rizk, Z.S., Alsharhan, A.S., 2003. Timing of recharge, and the origin, evolution and distribution of solutes in a hyperarid aquifer system. *Developments in Water Science* **50**, 295–312.